10-1-2021

HD 183579b: A Warm Sub-Neptune Transiting A Solar Twin Detected By *TESS*

T. Gan

M. Bedell

S. X. Wang

See next page for additional authors

Authors

T. Gan, M. Bedell, S. X. Wang, D. Foreman-Mackey, J. Meléndez, S. Mao, K. G. Stassun, S. B. Howell, C. Ziegler, R. A. Wittenmyer, C. Hellier, K. A. Collins, A. Shporer, G. R. Ricker, R. Vanderspek, D. W. Latham, S. Seager, J. N. Winn, J. M. Jenkins, B. C. Addison, S. Ballard, T. Barclay, J. L. Bean, B. P. Bowler, C. Briceño, I. J. M. Crossfield, J. Dittman, J. Horner, Eric L.N. Jensen, S. R. Kane, J. Kielkopf, L. Kreidberg, N. Law, A. W. Mann, M. W. Mengel, E. D. Morgan, J. Okumura, H. P. Osborn, M. Paegert, P. Plavchan, R. P. Schwarz, B. Shiao, J. C. Smith, L. Spina, C. G. Tinney, G. Torres, J. D. Twicken, M. Vezie, G. Wang, D. J. Wright, and H. Zhang

HD 183579b: a warm sub-Neptune transiting a solar twin detected by *TESS*

Tianjun Gan [,1]★ Megan Bedell,[2] Sharon Xuesong Wang,[1]★ Daniel Foreman-Mackey,[2] Jorge Meléndez,[3] Shude Mao,[1,4] Keivan G. Stassun [,5,6] Steve B. Howell,[7] Carl Ziegler,[8] Robert A. Wittenmyer,[9] Coel Hellier,[10] Karen A. Collins,[11] Avi Shporer,[12] George R. Ricker,[12] Roland Vanderspek,[12] David W. Latham,[11] Sara Seager,[12,13,14] Joshua N. Winn,[15] Jon M. Jenkins,[7] Brett C. Addison [,9] Sarah Ballard,[16] Thomas Barclay,[17,18] Jacob L. Bean,[19] Brendan P. Bowler,[20] César Briceño,[21] Ian J. M. Crossfield,[22] Jason Dittman,[11,23] Jonathan Horner [,9] Eric L. N. Jensen,[24] Stephen R. Kane,[25] John Kielkopf,[26] Laura Kreidberg,[11,23] Nicholas Law,[27] Andrew W. Mann,[27] Matthew W. Mengel [,9] Edward H. Morgan,[12] Jack Okumura,[9] Hugh P. Osborn,[12,28] Martin Paegert,[11] Peter Plavchan [,29] Richard P. Schwarz,[30] Bernie Shiao,[31] Jeffrey C. Smith,[7,32] Lorenzo Spina [,33] C. G. Tinney,[34] Guillermo Torres,[11] Joseph D. Twicken,[7,32] Michael Vezie,[12] Gavin Wang,[35,36] Duncan J. Wright[9] and Hui Zhang[37]

Affiliations are listed at the end of the paper

ABSTRACT

We report the discovery and characterization of a transiting warm sub-Neptune planet around the nearby bright ($V = 8.75$ mag, $K = 7.15$ mag) solar twin HD 183579, delivered by the *Transiting Exoplanet Survey Satellite* (*TESS*). The host star is located 56.8 ± 0.1 pc away with a radius of $R_* = 0.97 \pm 0.02\,R_\odot$ and a mass of $M_* = 1.03 \pm 0.05\,M_\odot$. We confirm the planetary nature by combining space and ground-based photometry, spectroscopy, and imaging. We find that HD 183579b (TOI-1055b) has a radius of $R_p = 3.53 \pm 0.13\,R_\oplus$ on a 17.47 d orbit with a mass of $M_p = 11.2 \pm 5.4\,M_\oplus$ (3σ mass upper limit of $27.4\,M_\oplus$). HD 183579b is the fifth brightest known sub-Neptune planet system in the sky, making it an excellent target for future studies of the interior structure and atmospheric properties. By performing a line-by-line differential analysis using the high-resolution and signal-to-noise ratio HARPS spectra, we find that HD 183579 joins the typical solar twin sample, without a statistically significant refractory element depletion.

Key words: planets and satellites: detection – planets and satellites: gaseous planets – planets and satellites: individual: (HD 183579, HIP 96160, TIC 320004517, TOI 1055) – stars: abundances – stars: solar type .

1 INTRODUCTION

After the first discovery of a hot Jupiter outside our Solar system (Mayor & Queloz 1995), exoplanet research has moved into a new era. Up to now, more than 4000 exoplanets have been confirmed.[1] Most giant planets have been found by successful ground surveys like HATNet (Bakos et al. 2004), SuperWASP (Pollacco et al. 2006), KELT (Pepper et al. 2007, 2012), and NGTS (Chazelas et al. 2012; Wheatley et al. 2018). Space mission conducting photometric transit surveys including *CoRoT* (Baglin et al. 2006), *Kepler* (Borucki et al. 2010), and *K2* (Howell et al. 2014) have led to the further detections of thousands of planets with size between Earth and Neptune. These diverse exoplanets are hosted by a similarly diverse set of stars. Among them, Sun-like stars (here defined as FGK main-sequence

stars) make up a significant fraction of known planet hosts. These systems can be seen as an intriguing opportunity to get a glimpse into alternate paths to that our own Solar system might have taken in its early formation, and they represent our best opportunity to discover a 'truly Earth-like' exoplanet that exists under conditions as similar as possible to our own planet (Horner et al. 2020; Kane et al. 2021).

Solar twins are an important sub-set of Sun-like stars. Typically defined by their extreme similarity to the Sun in fundamental spectroscopic properties ($T_{\rm eff}$ within 100 K, $\log g$ within 0.1 dex, and [Fe/H] within 0.1 dex of Solar values), these stars must by definition have such similar photospheric conditions to the Sun so that their spectra can be directly compared with minimal reliance on stellar atmospheric models. The result of a line-by-line differential spectroscopic analysis of a solar twin yields uniquely precise abundance measurements for the star and thereby for the star–planet system (see e.g. Bedell et al. 2018; Spina et al. 2018, who achieve 0.01 dex or 2 per cent precision on abundance measurements for over 30 elements). This is in direct contrast to a typical planet host star, whose abundances are expected to be limited by systematic

[1] https://exoplanetarchive.ipac.caltech.edu/

uncertainties to the level of 0.05 dex or more. Similarly precise measurements may be made of the star's age, mass, radius, and other fundamental properties by combining isochronal models with the spectroscopic measurements (Ramírez et al. 2014; Yana Galarza et al. 2016). It is worth emphasizing that these properties are measured with extreme precision (not necessarily accuracy) relative to the Sun, our most thoroughly characterized planet host. Planetary systems around solar twin stars are therefore useful both as individual well-characterized planets but also as a prime sample for comparative studies delving into any subtle differences between stars that host planets of different types. Unfortunately, the sample of solar twins with well-characterized planets around is still limited in number at present (e.g. *Kepler*-11, Lissauer et al. 2011; HIP 11915, Bedell et al. 2015; *K2*-231, Curtis et al. 2018; KELT-22, Labadie-Bartz et al. 2019), roughly 50 in total.

The *Transiting Exoplanet Survey Satellite* (*TESS*; Ricker et al. 2014, 2015), which performs an all-sky survey and focuses on small exoplanets orbiting nearby bright stars, will likely increase the sample of planets around solar twins significantly (Sullivan et al. 2015; Huang et al. 2018). During its two-year primary mission, *TESS* has detected over two thousand exoplanet candidates, the majority of which are suitable for follow-up observations, including mass measurements and atmospheric spectroscopy. This makes *TESS* planet candidates unlike most *Kepler* systems, which are too faint for these follow-up observation.

In this work, we present a warm sub-Neptune planet detected by *TESS* to orbit a solar twin star HD 183579. HD 183579 is a G2V star with a spectrum nearly identical to that of the Sun. The star has been studied extensively through a dedicated RV planet search and spectroscopic abundance survey targeting solar twin stars with the High Accuracy Radial velocity Planet Searcher spectrograph (HARPS; Mayor et al. 2003; Meléndez et al. 2015). The transiting planet, however, was not detected until *TESS* data became available.

This paper is organized as follows: In Section 2, we describe all observations. We characterize the host star HD 183579 in Section 3. Section 4 presents our analysis of the light curves and RV data. The lessons about comparison between HD 183579 and other similar systems are discussed in Section 5. In Section 6, we discuss insights into this system, prospects for further characterization via transmission spectroscopy, a search for additional planets, and a comparison with a recently published analysis of archival RVs of this target (Palatnick, Kipping & Yahalomi 2021). We conclude our findings in Section 7.

2 OBSERVATIONS

2.1 *TESS*

HD 183579 (TIC 320004517) was monitored by *TESS* with the two-minute cadence mode in Sector 13 during the primary mission and Sector 27 during the extended mission. The data were obtained between 2019 June 19th and 2019 July 18th, and between 2020 July 5th and 2020 July 30th, consisting of a total of 20 479 and 17 546 individual measurements, respectively.

The raw images were reduced using the Science Processing Operations Center (SPOC) pipeline (Jenkins et al. 2016), which was developed at NASA Ames Research Center based on the *Kepler* mission's science pipeline. After the systematic and dilution effects were corrected by the Presearch Data Conditioning (PDC; Smith et al. 2012; Stumpe et al. 2012, 2014) module, Transiting Planet Search (TPS; Jenkins 2002; Jenkins et al. 2017) was then performed to look for transit-like signals. HD 183579 was finally identified as a planet candidate in the *TESS* Object of Interest catalogue (TOI

1055.01) with a period of 17.47 d and a transit depth of 1259 ppm (Twicken et al. 2018; Li et al. 2019), and alerted on the MIT *TESS* Alerts portal.[2]

We downloaded the Presearch Data Conditioning Simple Aperture Photometry (PDCSAP) light curve from the Mikulski Archive for Space Telescopes (MAST[3]). After removing all measurements flagged for quality issues in SPOC to improve the precision, we applied the built-in routines of the `lightkurve` package (Lightkurve Collaboration 2018; Barentsen et al. 2019) to normalize the data and clip outliers above a $+5\sigma$ limit. These additional processing steps removed 904 and 802 points (4.4 and 4.6 per cent), with 19 575 and 16 744 measurements left for each sector.

To search for potential additional planets, we smoothed the light curve with a median filter and performed an independent transit search using the Box Least Square (BLS; Kovács, Zucker & Mazeh 2002) algorithm. We confirmed the ∼17 d signal reported by TPS. Except for that, we did not detect any other significant peaks existing in the periodogram.

After masking out all in-transit data, we detrended the light curve by fitting a Gaussian Process (GP) model with a simple Matern32 kernel using the `celerite` package (Foreman-Mackey et al. 2017). Fig. 1 shows the original SAP, PDCSAP, and the PDCSAP light curve after detrending. We used this reprocessed light curve in our further transit analysis.

2.2 Ground-based photometry

2.2.1 Las Cumbres Observatory (LCO)

The large pixel scale of *TESS* (21 arcsec pixel^{-1}, Ricker et al. 2014, 2015) may result in light contamination from stars close to the target, making nearby eclipsing binaries (NEB) a common source of *TESS* false positives (Brown 2003; Sullivan et al. 2015). To rule out the NEB scenario and confirm the event on target, we collected two ground-based follow-up observations using the Las Cumbres Observatory Global Telescope (LCOGT[4]) network (Brown et al. 2013). We used the *TESS* Transit Finder (TTF), which is a customized version of the `Tapir` software package (Jensen 2013), to schedule these time-series observations. The photometric observations were taken in the Pan-STARRS *Y* band with an exposure time of 35 s on 2020 June 27th and 2020 August 1st at Siding Spring Observatory (SSO), Australia and both were done with 1m telescopes. The Sinistro cameras have a 26′ × 26′ field of view as well as a plate scale of 0.389″ per pixel. The images were defocused and have stellar point-spread-functions (PSF) with a full width at half-maximum (FWHM) of ∼2″4 and ∼2″0, respectively. After the images were calibrated by the standard automatic BANZAI pipeline (McCully et al. 2018), we carried out photometric analysis using AstroImageJ (Collins et al. 2017). We excluded all nearby stars within 1 arcmin as the source causing the *TESS* signal with brightness difference down to $\Delta T \sim 7.5$ mag (see Fig. 2), and confirmed the signal on target. We summarize the observations in Table 1.

2.2.2 WASP

WASP-South, an array of eight cameras, was the Southern half of the WASP transit-search survey (Pollacco et al. 2006). The field of HD 183579 was observed in both 2013 and 2014, covering a span of 180

---

[2]https://tess.mit.edu/alerts/
[3]http://archive.stsci.edu/tess/
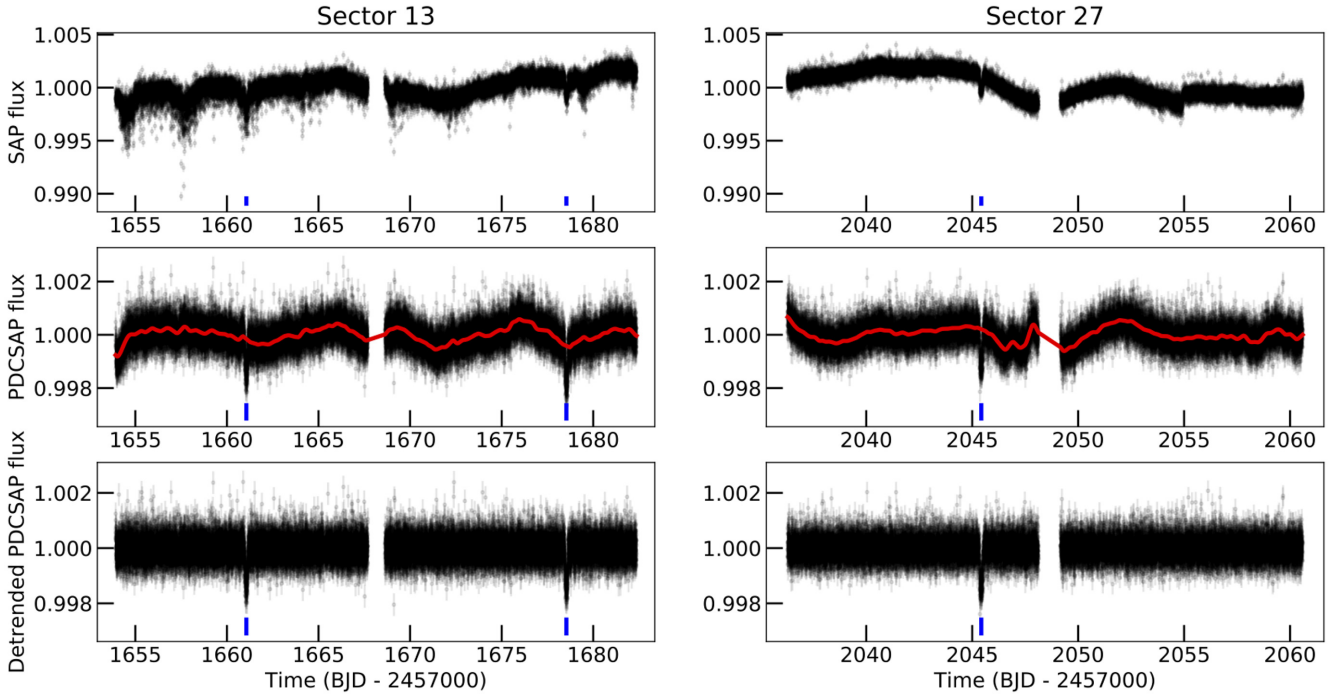[4]https://lco.global/

Figure 1. Top panels: The original *TESS* SAP light curves of HD 183579 from Sectors 13 and 27. Middle panels: The PDCSAP light curves of HD 183579 along with the best-fitting GP model shown as red solid lines. Bottom panels: The detrended PDCSAP light curves. The three transits of HD 183579b are marked in blue ticks.
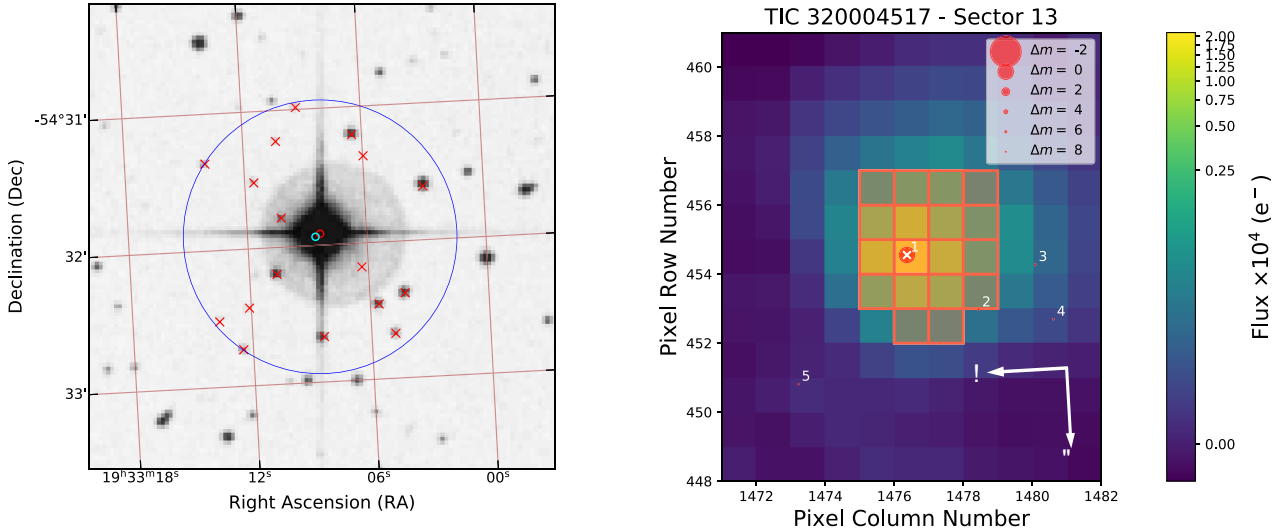

Figure 2. Left panel: The POSS2 blue image of HD 183579 taken in 1976. The centre red dot is the target star in this image and the cyan dot shows its current position. All stars (marked as red crosses) in 1 arcmin (the blue circle) are ruled out as the source that causes the *TESS* detection based on their brightness and the NEB analysis of LCO photometry. Right panel: Target pixel file (TPF) of HD 183579 in *TESS* Sector 13 (created with `tpfplotter`, Aller et al. 2020). Different sizes of red circles represent different magnitudes in contrast with HD 183579 (Δm). The red-square region represents the aperture used to extract the photometry by SPOC. The light contamination from nearby stars is negligible (see Section 4.1).

Table 1. Summary of ground-based photometric observations for HD 183579.

Facility	Date	Total exposures	Exposure time (s)	Filter	Coverage	Label
LCO 1m SSO Sinistro	2020 June 27	224	35	Pan-STARRS Y	egress	LCOA
LCO 1m SSO Sinistro	2020 Aug 1	274	35	Pan-STARRS Y	egress	LCOB

nights in each year with a typical 10-min cadence on clear nights, and accumulating 52 000 data points. WASP-South was equipped with 85-mm, f/1.2 lenses giving a photometric extraction aperture with a 112-arcsec radius. All other stars within this aperture are >5 mag fainter.

2.3 High-resolution spectroscopy

2.3.1 HARPS

HD 183579 was observed 56 times by the HARPS (Mayor et al. 2003) on the ESO 3.6 m telescope at La Silla Observatory in Chile between 2011 and 2019. The bulk of these observations were made as part of a dedicated blind planet search targeting solar twins (P.I. Meléndez). All observations were carried out in high-accuracy mode with a spectral resolution $R \sim 115\,000$. The median SNR is 108 pixel^{-1} at 600 nm.

We extracted the radial velocity (RV) measurements, chromatic RV index (CRX), and differential line width (dLW) using the publicly available SpEctrum Radial Velocity AnaLyser pipeline (SERVAL; Zechmeister et al. 2018). Additional diagnostics including the inverse bisector span (BIS) and FWHM for the line profile of the average spectral features were extracted by the standard HARPS pipeline using a cross-correlation technique with a solar-type mask (Pepe et al. 2002). These diagnostics are commonly used as stellar activity tracers, since they quantify the line distortions which mimic Doppler shifts.

In addition to these activity indicators, we also derived the S_{HK} measurement, which quantifies the strength of emission in the cores of the Ca II H&K lines. These were measured and corrected to the standard Mount Wilson scaling using the procedure outlined in Lovis et al. (2011). Measured S_{HK} values and photon-noise-based uncertainties along with the pipeline values of RV, BIS, FWHM, CRX, and dLW are publicly available on ExoFOP-TESS.[5]

We dropped one observation (BJD=245 7588.767) from the analysis because its BIS and FWHM measurements were significant outliers (>5σ) from the general distribution, pointing to potential issues with the data reduction and RV extraction.

2.3.2 Minerva-Australis

Minerva-Australis is an array of four PlaneWave CDK700 telescopes located at the Mt Kent Observatory in Queensland, Australia, fully dedicated to the precise RV follow-up of *TESS* candidates (e.g. Jordán et al. 2020; Addison et al. 2021, 2020). The four telescopes can be simultaneously fibre-fed to a single KiwiSpec R4-100 high-resolution ($R = 80\,000$) spectrograph (Barnes et al. 2012; Addison et al. 2019). HD 183579 was monitored by Minerva-Australis using up to four telescopes in the array between 2020 April 19 and 2020 June 1. Each epoch consists of one or two 30-min exposures. Telescopes 1, 3, 4, and 5 (denoted as MA, MB, MC, and MD) obtained 5, 8, 15, and 5 epochs respectively. Radial velocities for the observations are derived for each telescope by cross-correlation, where the template being matched is the mean spectrum of each telescope. A simultaneous quartz-illuminated iodine cell in the calibration fibres provides the wavelength calibration and corrects for instrumental variations. We converted all time-stamps of our measurements from JD to BJD using barycorr (Wright

& Eastman 2014). We list all RVs from HARPS and MINERVA-Australis in Tables A1 and A2.

2.4 High angular resolution imaging

High-angular resolution imaging is needed to search for nearby sources that can contaminate the *TESS* photometry, resulting in an underestimated planetary radius, or other sources of astrophysical false positives, such as background eclipsing binaries.

2.4.1 Gemini-South

We observed HD 183579 to probe for companion stars on 12 September 2019 UT using the Zorro instrument mounted on the 8 m Gemini South telescope, located on Cerro Pachón in Chile. Zorro uses speckle imaging to simultaneously observe diffraction-limited images at 562 nm (0.017 arcsec) and 832 nm (0.028 arcsec). Our data set consisted of three 1000×60 ms exposure images simultaneously obtained in both bandpasses, followed by a single 1000×60 ms image, also in both bandpasses, of a PSF standard star.

Following the procedures outlined in Howell et al. (2011), we combined all images and subjected them to Fourier analysis, and produce re-constructed imagery from which 5σ contrast curves are derived in each passband (Fig. 3). Our data reveal HD 183579 to be a single star to contrast limits of 5–8 mag within the spatial limits of 1.0/1.6 AU (562/832 nm respectively) out to 57 AU.

2.4.2 SOAR

We also searched for stellar companions to HD 183579 with speckle imaging on the 4.1-m Southern Astrophysical Research (SOAR) telescope (Tokovinin 2018) on 2020 October 31 UT, observing in Cousins *I* band, a similar visible bandpass as *TESS*. More details of the observations are available in Ziegler et al. (2020). The 5σ detection sensitivity and speckle autocorrelation functions from the observations are shown in the right-hand panel of Fig. 3. No nearby stars were detected within 3 arcsec of HD 183579 in the SOAR observations.

3 STELLAR PROPERTIES

3.1 Stellar characterization

We first derived T_{eff}, R_*, and iron abundance [Fe/H] from the spectroscopic data. By utilizing the SpecMatch-Emp package (Yee, Petigura & von Braun 2017), we matched the co-added HARPS spectrum to a high resolution spectroscopic library, which contains 404 well-characterized stars, following Hirano et al. (2018). We found $T_{eff} = 5678 \pm 110$ K, $R_* = 0.988 \pm 0.100\,R_\odot$ and [Fe/H] = -0.07 ± 0.09 dex. This is in good agreement with the literature values of $T_{eff} = 5798 \pm 4$ K, $\log g = 4.480 \pm 0.012$ dex, and [Fe/H] = -0.036 ± 0.003 dex, as derived by Spina et al. (2018) using the same co-added HARPS observations with a strictly differential line-by-line equivalent width technique.

For comparison, we then performed an analysis of the broad-band spectral energy distribution (SED) together with the *Gaia* EDR3 parallax (Gaia Collaboration 2021) in order to determine an empirical measurement of the stellar radius, following the procedures described in Stassun & Torres (2016) and Stassun, Collins & Gaudi (2017), Stassun et al. (2018a). We gathered the FUV, NUV magnitudes from *GALEX* (Morrissey et al. 2007), the B_T, V_T magnitudes from *Tycho-2*
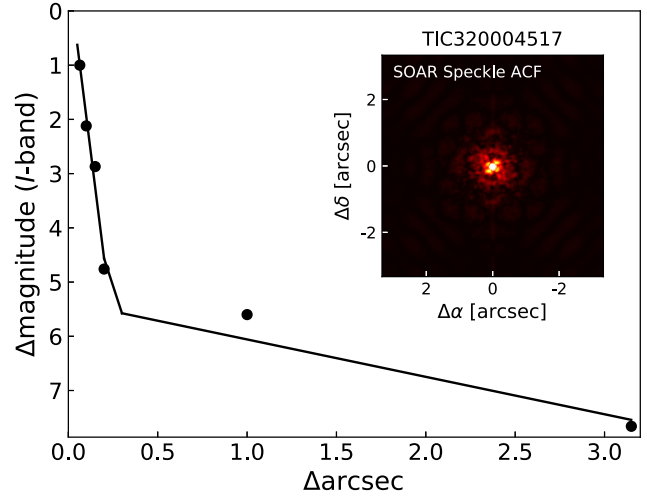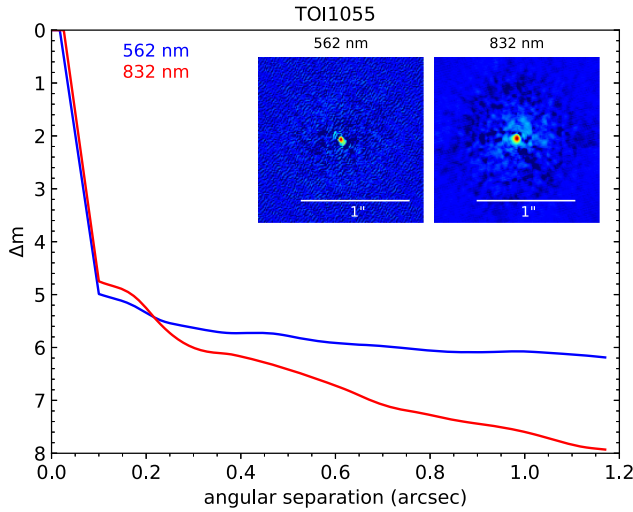
Figure 3. Left panel: Zorro speckle imaging and 5σ contrast curves of HD 183579 at 562 nm and 832. The data reveal that no companion star is detected within the spatial limits of 1 AU out to 57 AU with a Δm of 5 to 8. Right panel: Speckle ACF obtained in the *I* band using SOAR. The 5σ contrast curve for HD 183579 is shown by the black points. Black solid line corresponds to the linear fit of the data, at separations smaller and larger than ~0.2 arcsec.
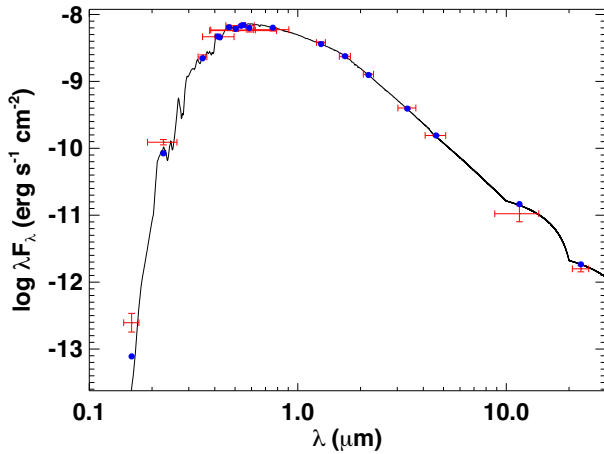

Figure 4. The best SED fit for HD 183579. The Red symbols show the observed photometric measurements, where the horizontal bars represent the effective width of the passband. The Blue points are the predicted integrated fluxes at the corresponding bandpass. The black line represents the best-fitting NextGen atmosphere model.

(Høg et al. 2000), the Strömgren *u*, *v*, *b*, *y* magnitudes from Paunzen (2015), the *J*, *H*, K_S magnitudes from 2MASS point source catalogue (Cutri et al. 2003; Skrutskie et al. 2006), four *Wide-field Infrared Survey Explorer* (*WISE*) magnitudes (Wright et al. 2010), and three *Gaia* magnitudes G, G_{BP}, G_{RP}. Together, the available photometry spans the full stellar SED over the wavelength range 0.15–22 μm (see Fig. 4).

We performed a fit using the Kurucz stellar atmosphere models, with the priors on effective temperature (T_{eff}), surface gravity (log *g*) and metallicity ([Fe/H]) from the spectroscopic analysis. The remaining free parameter is the extinction (A_V), which we limited to the maximum permitted for the star's line of sight from the dust maps (Schlegel, Finkbeiner & Davis 1998). The best-fitting SED is shown in Fig. 4 with a reduced $\chi^2 = 1.4$ (excluding the *GALEX* UV measurements, which indicate mild chromospheric activity; see below) and $A_V = 0.01 \pm 0.01$. Integrating the model SED gives a

bolometric flux at Earth of $F_{bol} = 9.32 \pm 0.11 \times 10^{-9}$ erg s^{-1} cm^{-2}. Taking the F_{bol} and T_{eff} together with the *Gaia* parallax, we obtained a stellar radius of $R_* = 0.972 \pm 0.014 R_\odot$, which agrees with the previous result within 1σ.

We computed an empirical estimate of the stellar mass from this R_* together with the spectroscopic log *g*, from which we obtained $M_* = 1.03 \pm 0.05 M_\odot$. This is consistent with that estimated via the eclipsing-binary based relations of Torres, Andersen & Giménez (2010), which gives $M_* = 1.04 \pm 0.06 M_\odot$.

Taking all the results above into consideration, we finally adopted the weighted mean values of effective temperature T_{eff}, stellar radius R_* and stellar mass M_*. Combining the expected stellar radius with mass, we found a mean stellar density of $\rho_* = 1.58 \pm 0.16$ g cm^{-3}.

Following Johnson & Soderblom (1987), we adopted the astrometric values (ϖ, μ_α, μ_δ) from *Gaia* EDR3 (Gaia Collaboration 2021) as well as systemic RV taken from *Gaia* DR2 (Gaia Collaboration 2018), and computed the 3D Galactic space motion of (U_{LSR}, V_{LSR}, W_{LSR}) = (−23.10 ± 0.19, 1.53 ± 0.06, −14.14 ± 0.10) km s^{-1}, all of which are relative to the LSR. Building on the kinematic calculation, we then determined the relative probability P_{thick}/P_{thin} of HD 183579 to be in the thick and thin disks (Bensby, Feltzing & Lundström 2003; Bensby, Feltzing & Oey 2014). We obtained $P_{thick}/P_{thin} = 0.01$, indicating a thin-disc origin. We further employed the galpy package (Bovy 2015) to estimate the maximal height Z_{max} of HD 183579 above the Galactic plane, along with the 'MWPotential2014' Galactic potential following Gan et al. (2020). We find HD 183579 has a Z_{max} of ~213 pc, which agrees with our thin-disc conclusion.

The *GALEX* photometry suggests a mild amount of chromospheric activity. Indeed, Lorenzo-Oliveira et al. (2018) reported a spectroscopically measured log $R'_{HK} = -4.89 \pm 0.02$, consistent with a mild level of activity. Based on the Yonsei-Yale isochrones, Spina et al. (2018) found that HD 183579 has an age of 2.6 ± 0.5 Gyr. We list all final adopted stellar parameter values in Table 2.

3.2 Stellar rotation

The *TESS* PDCSAP light curve from sector 13 shows a clear variation with a time-scale of ~9.5 d, which implies a relatively high stellar

Table 2. Stellar parameters of HD 183579.

Parameter	Value	Reference
Star ID		
TIC	320004517	
TOI	1055	
HIP	96160	
Astrometric properties		
α (*J*2000)	19:33:08.58	
δ (*J*2000)	-54:31:56.50	
ϖ (mas)	17.609 ± 0.016	*Gaia* EDR3
μ_α (mas yr^{-1})	108.32 ± 0.01	*Gaia* EDR3
μ_δ (mas yr^{-1})	-82.71 ± 0.01	*Gaia* EDR3
RV (km s^{-1})	-15.8 ± 0.2	*Gaia* DR2
Photometric properties		
TESS (mag)	8.089 ± 0.006	TIC V8[a]
G (mag)	8.5265 ± 0.0002	*Gaia* EDR3
G_{BP} (mag)	8.843 ± 0.001	*Gaia* EDR3
G_{RP} (mag)	8.037 ± 0.002	*Gaia* EDR3
B_T (mag)	9.477 ± 0.019	Tycho-2
V_T (mag)	8.750 ± 0.013	Tycho-2
J (mag)	7.518 ± 0.023	2MASS
H (mag)	7.231 ± 0.047	2MASS
K_S (mag)	7.150 ± 0.027	2MASS
*W*1 (mag)	7.090 ± 0.043	*WISE*
*W*2 (mag)	7.137 ± 0.020	*WISE*
*W*3 (mag)	7.138 ± 0.019	*WISE*
*W*4 (mag)	7.040 ± 0.114	*WISE*
Derived parameters		
log g_* (cgs)	4.47 ± 0.03	This work
[Fe/H] (dex)	-0.07 ± 0.09	This work
Distance (pc)	56.79 ± 0.06	This work
U_{LSR} (km s^{-1})	-23.10 ± 0.19	This work
V_{LSR} (km s^{-1})	1.53 ± 0.06	This work
W_{LSR} (km s^{-1})	-14.14 ± 0.10	This work
T_{eff}^b (K)	5706 ± 110	This work
M_* ($M_\odot$)	1.034 ± 0.050	This work
R_* ($R_\odot$)	0.974 ± 0.015	This work
ρ_* (g cm^{-3})	1.58 ± 0.16	This work
P_{rot} (d)	23.2 ± 3.7	This work
A_V (mag)	0.01 ± 0.01	This work
Age (Gyr)	2.6 ± 0.5	Spina et al. (2018)

[a]Stassun et al. (2018b, 2019);
[b]We take the average values of T_{eff}, M_*, and R_* here (see Section 3.1).

rotation speed. However, this periodic signature is not shown in the corresponding SAP light curve (see Fig. 1). Additionally, the subsequent light curve from the extended mission does not have a similar trend. We show below that this ∼9.5 d signal is more likely due to instrumental systematic errors instead of real stellar variability.

First, we estimated the rotation period $P_{rot}/\sin i = 24.4 \pm 2.6$ d based on the stellar radius R_* together with the spectroscopically determined rotational velocity $v\sin i = 2.1 \pm 0.2$ km s^{-1} (Soto & Jenkins 2018). Assuming $\sin i = 1$, this is consistent with the value $P_{rot} = 23.2 \pm 3.7$ d inferred using the empirical activity-rotation relation from Mamajek & Hillenbrand (2008) according to gyrochronology (Barnes 2007; Meibom, Mathieu & Stassun 2009; Curtis et al. 2019).

Furthermore, McQuillan, Mazeh & Aigrain (2014) analysed the rotation periods of main-sequence stars below 6500 K based on 3 yr of data from the *Kepler* space mission. Our derived rotation period P_{rot} 23.2 ± 3.7 d of HD 183579 agrees with the typical value ∼20 d of solar-like stars with a T_{eff} of ∼5700 K (see figs 4 and 5 in McQuillan et al. 2014).
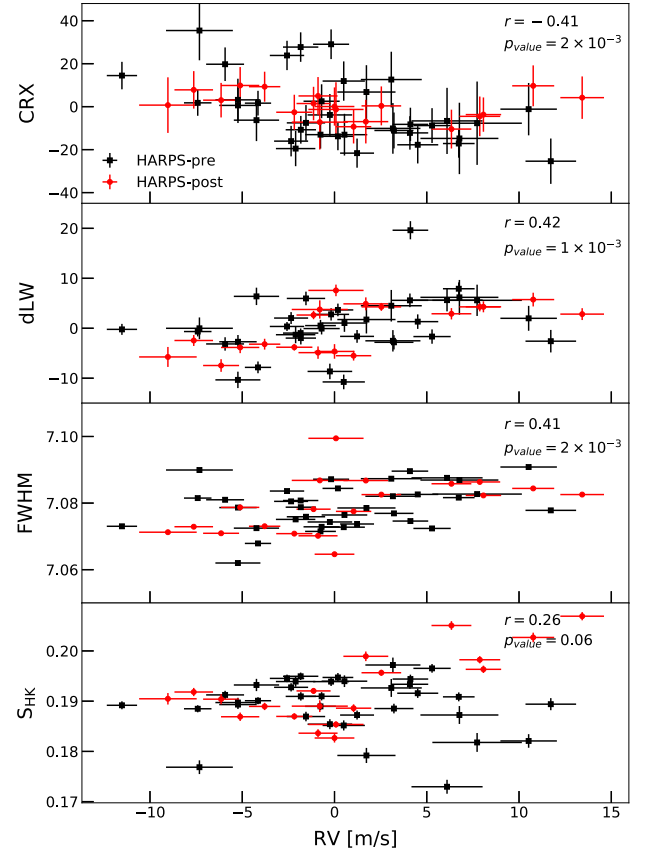

Figure 5. Correlations between HARPS RVs and activity indicators (CRX, dLW, FWHM, and S_{HK}). Different colours represent HARPS pre-upgrade/post-upgrade data. The Pearson's correlation indices and the corresponding *p*-values are shown in the upper right. In each plot we have subtracted the median value of both RV and the activity indices. The clear correlations indicate that stellar activity has an effect on the Doppler signals (see Section 3.2).

We also investigated the rotational modulation in the WASP accumulated data as archival long-term light curve could provide information on stellar rotation features. However, we did not find significant signals likely due to the influence of lunar stray light in the 23–27 d regime.

Finally, we performed a frequency analysis for the HARPS activity indicators (CRX, dLW, bisector span, FWHM, and S_{HK}). One instrumental effect must be accounted for here: In June 2015, the HARPS optical fibres were replaced as part of a major instrument upgrade, leaving an effective offset between RVs and other line profile-sensitive components measured before and after the upgrade (Lo Curto et al. 2015). For this initial inspection, we calculated the median values for both RVs and each indicator, and subtracted the corresponding offset between pre-upgrade and post-upgrade data. Because of the sparse sampling, we did not see any significant periodic signals, therefore, we do not present the periodograms here. However, we found strong correlations between RVs and CRX, dLW and FWHM ($r = -0.41$, *p*-value $= 2 \times 10^{-3}$; $r = 0.42$, *p*-value $= 1 \times 10^{-3}$; $r = 0.41$, *p*-value $= 2 \times 10^{-3}$) and weak correlations between RVs and S_{HK} ($r = 0.26$, *p*-value $= 0.06$) as shown in Fig. 5, which motivated us to take the stellar activity into consideration in the following RV modelling (see Section 4.2).

Table 3. Model parameters, prior settings, and the best-fitting values for the *TESS* and ground-based light curves of HD 183579.

Parameter	Best-fitting value	Prior	Description
Planetary parameters			
P_b (d)	$17.47128^{+0.00005}_{-0.00005}$	$\mathcal{N}^a$ $(17.4, 0.1^2)$	Orbital period of HD 183579b.
$T_{0,b}$ (BJD-245 7000)	$1661.06295^{+0.00070}_{-0.00071}$	$\mathcal{N}$ $(1661.1, 0.1^2)$	Mid-transit time of HD 183579b.
$r_{1,b}$	$0.613^{+0.133}_{-0.127}$	$\mathcal{U}^b$ $(0, 1)$	Parametrization for p and b.
$r_{2,b}$	$0.03319^{+0.00069}_{-0.00056}$	$\mathcal{U}$ $(0, 1)$	Parametrization for p and b.
e_b	0	Fixed	Orbital eccentricity of HD 183579b.
ω_b (deg)	90	Fixed	Argument of periapsis of HD 183579b.
TESS photometry parameters			
D_{TESS}	1	Fixed	*TESS* photometric dilution factor.
M_{TESS}	$-0.0000003^{+0.000002}_{-0.000002}$	$\mathcal{N}$ $(0, 0.1^2)$	Mean out-of-transit flux of *TESS* photometry.
σ_{TESS} (ppm)	110^{+5}_{-5}	$\mathcal{J}^c$ $(10^{-6}, 10^6)$	*TESS* additive photometric jitter term.
q_1	$0.32^{+0.18}_{-0.12}$	$\mathcal{U}$ $(0, 1)$	Quadratic limb darkening coefficient.
q_2	$0.26^{+0.32}_{-0.17}$	$\mathcal{U}$ $(0, 1)$	Quadratic limb darkening coefficient.
LCOA photometry parameters			
D_{LCOA}	1	Fixed	LCOA photometric dilution factor.
M_{LCOA}	$-0.0006^{+0.00008}_{-0.00007}$	$\mathcal{N}$ $(0, 0.1^2)$	Mean out-of-transit flux of LCOA photometry.
σ_{LCOA} (ppm)	520^{+147}_{-234}	$\mathcal{J}$ $(0.1, 10^5)$	LCOA additive photometric jitter term.
q_{LCOA}	$0.42^{+0.07}_{-0.09}$	$\mathcal{N}$ $(0.37, 0.1^2)$	Linear limb darkening coefficient.
LCOB photometry parameters			
D_{LCOB}	1	Fixed	LCOB photometric dilution factor.
M_{LCOB}	$-0.0006^{+0.00008}_{-0.00008}$	$\mathcal{N}$ $(0, 0.1^2)$	Mean out-of-transit flux of LCOB photometry.
σ_{LCOB} (ppm)	817^{+87}_{-85}	$\mathcal{J}$ $(0.1, 10^5)$	LCOB additive photometric jitter term.
q_{LCOB}	$0.35^{+0.09}_{-0.08}$	$\mathcal{N}$ $(0.37, 0.1^2)$	Linear limb darkening coefficient.
Stellar parameters			
ρ_* (kg m^{-3})	1514^{+353}_{-535}	$\mathcal{J}$ $(100, 100^2)$	Stellar density.
Derived parameters			
R_{p}/R_*	$0.03319^{+0.00069}_{-0.00056}$		Planet radius in units of stellar radii.
R_{p} ($R_\oplus$)	$3.53^{+0.13}_{-0.11}$		Planet radius.
b	$0.42^{+0.20}_{-0.19}$		Impact Parameter.
a/R_*	$29.0^{+2.1}_{-2.8}$		Semi-major axis in units of stellar radii.
a (AU)	$0.13^{+0.01}_{-0.01}$		Semi-major axis.
i (deg)	$89.17^{+0.40}_{-0.58}$		Inclination angle.
T_{eq}^d (K)	748^{+55}_{-40}		Equilibrium temperature.

[a] $\mathcal{N}(\mu, \sigma^2)$ means a normal prior with mean μ and standard deviation σ;

[b] $\mathcal{U}$(a, b) stands for a uniform prior ranging from a to b;

[c] $\mathcal{J}$(a, b) stands for a Jeffrey's prior ranging from a to b;

[d] We assume there is no heat distribution between the dayside and nightside, and that the albedo is zero.

4 ANALYSIS

4.1 Photometric analysis

We utilized the `juliet` package (Espinoza, Kossakowski & Brahm 2019) to perform a joint-fit of both space and ground-based light curves. The transit is modelled by `batman` (Kreidberg 2015). We applied the dynamic nested sampling approach to determine the posterior probability distribution of the system parameters using the public package `dynesty` (Higson et al. 2019; Speagle 2020).

We retrieved a list of nearby stars of HD 183579 ($G_{\text{rp}} = 8.037$ mag) within 30 arcsec in *Gaia* EDR3 to estimate the flux dilution effect in the ground-based photometries (Espinoza et al. 2019). Three faint stars with $G_{\text{rp}} > 17.4$ mag are found located at >25 arcsec away from HD 183579. As the nearby stars are faint and relatively distant, these stars should make minor contribution to the contaminated flux, which is consistent with the small contamination ratio $A_{\text{D}} = 0.001$ reported in the *TESS* input catalogue (TIC) V8 (Stassun et al. 2018b, 2019).

Thus, we fixed the dilution factors D_{LCO} equal to 1 but considered individual instrument offsets.

We adopted Gaussian priors for the period P_b and mid-transit time t_0 based on the results from the BLS search. `juliet` applies the new parametrizations r_1 and r_2 to sample points (Espinoza 2018), for which we set uniform priors between 0 and 1. We adopted a quadratic limb-darkening law for *TESS* photometry and uniformly sampled the coefficients (q_1 and q_2, Kipping 2013). For ground-based data, we used a linear law instead to parametrize the limb-darkening effect and placed a Gaussian prior on the coefficient, centred at the theoretical estimate derived from the LDTK package (Husser et al. 2013; Parviainen & Aigrain 2015) with a 1σ value of 0.1. We fit a circular orbit for HD 183579b with a non-informative log-uniform prior set on the stellar density. For each instrument, we included a flux jitter term to account for the white noise. The results of the fit along with the corresponding prior settings are listed in Table 3. We present the best-fitting models in Fig. 6.
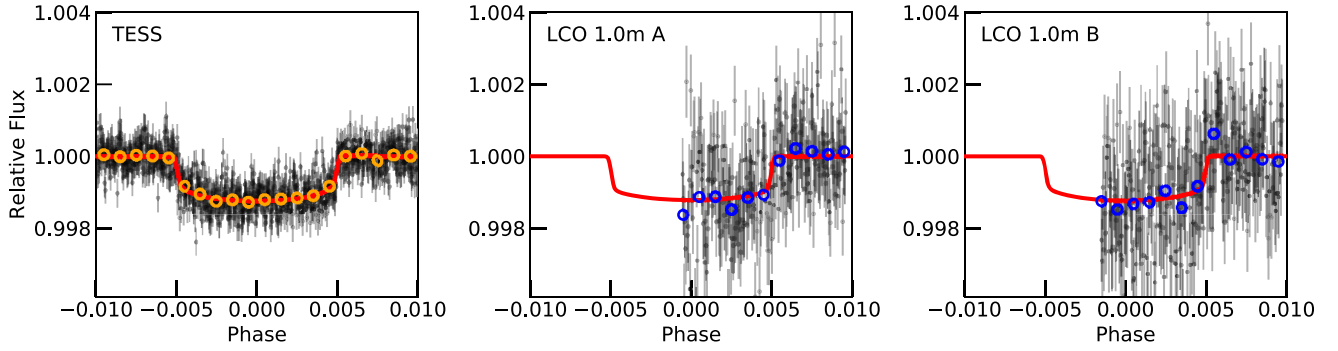
Figure 6. Phase-folded transits of HD 183579b for all available photometric instruments. *TESS* data are presented in the left panel. Two LCO 1m/Sinistro light curves obtained in the Pan-STARRS *Y* band are shown in the middle and right panels. The orange and blue points represent the binned light curves. The best-fitting models are shown as red solid lines.

4.2 RV modelling

We chose to fit the RVs independently of the transit fit with priors informed by the photometric analysis. We employed the `forecaster` package to predict the mass of HD 183579b (Chen & Kipping 2017). We obtained $12.0^{+9.0}_{-5.3}$ $M_\oplus$ based on the probabilistic mass–radius relation, which corresponds to a radial velocity semi-amplitude K_b of $\sim 2.8^{+2.2}_{-1.2}$ m s^{-1}, assuming a circular orbit. This expected RV signal is beyond the detection capability of MINERVA (typical error bar is ~ 7 m s^{-1}). Hence, we chose to analyse the HARPS-only data set first to avoid the MINERVA RVs obscuring the signal, then combine the additional MINERVA data and perform a joint-fit.

4.2.1 HARPS-only

We fit the HARPS-only RVs independent of the transit modelling with priors coming from the best-fitting transit ephemeris. `Juliet` utilizes the `radvel` algorithm to create the Keplerian model (Fulton et al. 2018) for the RV time-series data. We compared different RV models based on the Bayesian model log evidence (ln Z) calculated by the `dynesty` package. In general, a model is favoured if $\Delta \ln Z > 2$ compared with the other, and strongly supported if $\Delta \ln Z > 5$ (Trotta 2008).

We first performed a simple 1-planet (i.e. HD 183579b) Keplerian orbit fit with uniform priors on $e \sin \omega$ and $e \cos \omega$. We treated the HARPS-pre and HARPS-post data as from two different instruments and included the RV offset and the RV jitter terms for each set of data. We obtained $e = 0.49 \pm 0.30$, indicating the current RVs are insufficient to constrain the eccentricity. Moreover, compared with a circular orbit model, we found the Bayesian evidence is not significantly stronger for the eccentric model ($\Delta \ln Z = \ln Z_{ecc} - \ln Z_{circ} < 1$). Thus we chose to fix the orbital eccentricity to 0 in all our runs and considered this 1-planet circular orbit model as our base model (hereafter BM; 1pl). We further compared the ln Z of the BM model and a no-planet model (np), and we found a significant improvement ($\Delta \ln Z = \ln Z_{BM} - \ln Z_{np} = 13$), supporting the existence of the planet. The BM model gives $K_b = 2.3^{+1.1}_{-1.0}$ m s^{-1}, which leads to a marginal mass measurement of 9.5 ± 4.5 $M_\oplus$. We show all HARPS RV data along with best-fitting model in Fig. 7. The RV periodogram does not show an obvious planet signal at ~ 17 d or any other significant peaks with FAP < 0.1 per cent due to the poor sampling. However, subtracting the best-fitting BM model resulted in a forest of peaks between 22.6 d and 99.2 d with FAP < 0.1 per cent in the GLS periodogram of residuals, which may

arise from additional planets in the system or from noise that was not accounted for in our model (e.g. stellar activity).

To investigate the source of these new peaks we identified in the GLS periodogram (see Fig. 7), we fit a BM+1pl (HD 183579b + a potential outer planet) model, allowing the period P_c vary uniformly between 20 d and 110 d along with a wide uniform prior on the RV semi-amplitude K_c. However, we did not find any convergences in the $P_c - K_c$ space, indicating that there is no evidence for the existence of another outer non-transiting planet within the period range. This is also confirmed by the Bayesian model log evidence, which only shows a negligible improvement compared with the BM model ($\Delta \ln Z = \ln Z_{BM + 1pl} - \ln Z_{BM} = 2$).

If stellar activity signals are present in the data, from surface features rotating across the star or from longer-term variations in the net convective blueshift suppression, they could also add peaks to the periodogram. In particular, the phase incoherence of activity signals due to constantly evolving surface features over the long duration of RV observations will contribute excess power in disordered structures around the rotation period and its harmonics, which unfortunately coincide with the region of period space we wish to search. With all of this in mind, we explored two approaches to deal with the stellar activity effect on the Doppler signals.

First, we modelled the RVs using Gaussian Process regression (BM+GP) with a quasi-periodic kernel formulated by Foreman-Mackey et al. (2017):

$$k_{i,j}(\tau) = \frac{B}{2 + C} e^{-\tau/L} \left[\cos \left(\frac{2\pi\tau}{P_{rot}} \right) + (1 + C) \right], \quad (1)$$

where B defines the GP covariance amplitude, C is a balance parameter for the periodic and the non-periodic parts, $\tau = |t_i - t_j|$ is the time lag between data points i and j, and L and P_{rot} represent the coherence time-scale and the stellar rotational period, respectively. We adopted uninformative, wide log-uniform priors to the GP parameters except for the periodic time-scale P_{rot}, where we chose a narrow Gaussian prior centring at 23.2 d with $\sigma_{P_{rot}} = 4$ d according to our findings in Section 3.2. We obtained $K_b = 4.3 \pm 1.0$ m s^{-1}, which is consistent with our estimate from BM+1pl within 2σ. Although we noticed a significant enhancement of ln Z ($\Delta \ln Z = \ln Z_{BM + GP} - \ln Z_{BM} = 8$), we suspected the GP model might have overfitted the RV data. The expected stellar rotation time-scale (~ 23 d) is much smaller than the total RV baseline (>2800 d) and the current RV data points are too sparse, which implies the stellar activity signal is not well sampled, making GP not robust in such a challenging case. Comparing with a GP-only model, we also found
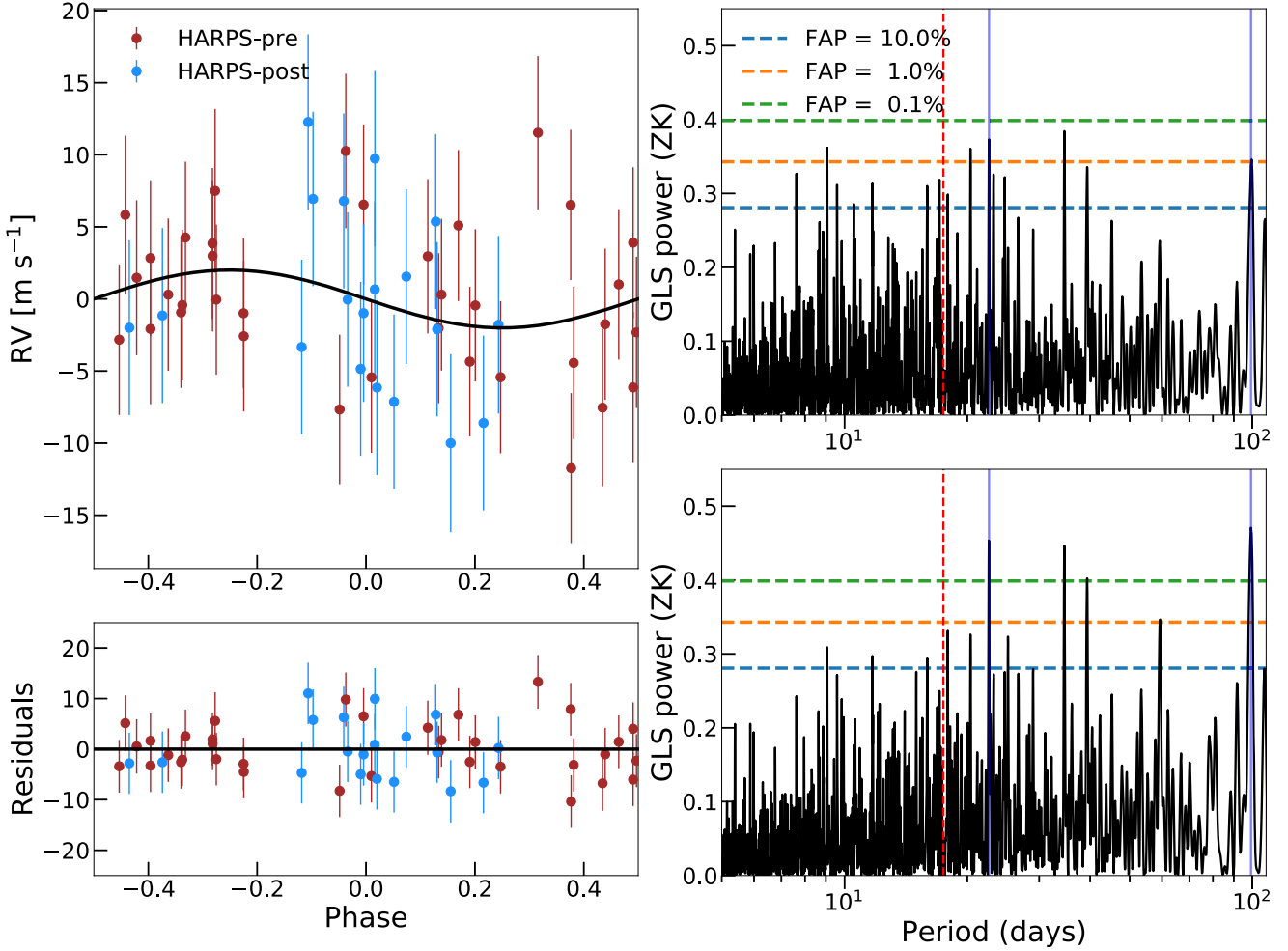
Figure 7. Top left panel: The phase-folded HARPS RVs of HD 183579. The best-fitting base model is shown as a black solid line. Bottom left panel: RV residuals after subtracting the best-fitting Keplerian model. The error bars are the quadrature sum of the instrument jitter term and the measurement uncertainties for all RVs. Right panels: The GLS periodograms of the total HARPS RV data (top) and the residuals (bottom) after adjusting for the RV offsets between different instruments using the best-fitting values from our base model. The 10, 1, and 0.1 per cent FAP levels are shown as horizontal dashed lines. The red vertical dashed line represents the period of HD 183579b ($P_b = 17.47$ d) derived from the light-curve fit. The periodogram of the RV residuals shows up a forest of peaks between 22.6 and 99.2 d (two blue vertical lines) which may be due to the stellar activity (see Section 4.2).

a $\ln Z$ improvement of the BM+GP model ($\Delta \ln Z = \ln Z_{BM+GP} - \ln Z_{GP} = 5$).

We then constructed a simple and fast-to-compute model by involving the activity indicators into the analysis (BM+FWHM). We first tested this option by checking to see whether accounting for activity indicators via linear correlations in the RV analysis would reduce the RV noise to the point that the planet signal could be seen in the periodogram. We adopted a linear relationship between RV and the HARPS FWHM, which was previously shown to correlate significantly with RV (Fig. 5). We also added in a quadratic trend component to account for long-term changes in the RVs due to either the evolving magnetic activity cycle or undetected long-period companions. With this more advanced model, we constructed a *log-likelihood periodogram*. This approach is a simple and efficient way of searching frequency space while taking certain systematic noise sources into account, and follows the methodology behind the Systematics-Insensitive Periodogram introduced for *Kepler* transit searches by Angus, Foreman-Mackey & Johnson (2016). It is analogous to the Bayesian generalized Lomb-Scargle periodogram introduced by Mortier et al. (2015), but contains additional noise

terms. Specifically, in our application the model prediction is that for any time t_n with corresponding FWHM measurement w_n, the RV y_n is given by

$$y_n = ax_n^2 + bx_n + c_n + dw_n + K \sin\left(\frac{2\pi}{P}t_n\right)$$
$$+ H \cos\left(\frac{2\pi}{P}t_n\right) + \text{noise}, \qquad (2)$$

where x_n is a normalized relative time:

$$x_n = \frac{t_n - \langle \mathbf{t} \rangle}{\max(\mathbf{t}) - \min(\mathbf{t})}, \qquad (3)$$

the baseline term c_n is comprised of two possible values based on whether observation n was taken before or after HARPS upgrade time t_{upgrade}:

$$c_n = c_1 \delta_n + c_2 \neg \delta_n, \qquad (4)$$

with δ_n set to 1 for pre-upgrade data and 0 for post-upgrade data. The variables (a, b, c_1, c_2, d, K, H, P) are unknowns to be constrained from the data. At any given value of the orbital period P, this
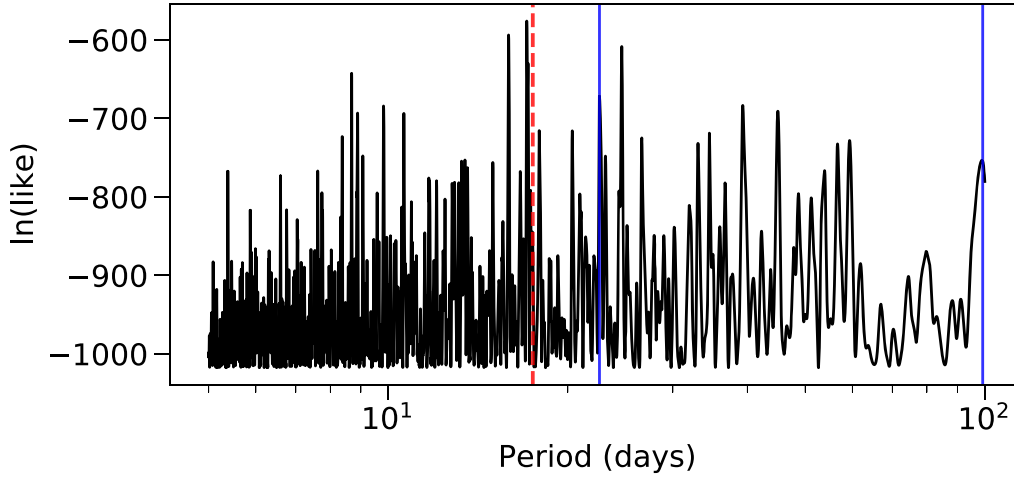
Figure 8. Periodogram of the HARPS RVs employing the log-likelihood periodogram method described in the text. Vertical lines mark the period of HD 183579b (red dashed line) and the bounds of the forest of peaks seen in Fig. 7 (blue solid lines). After accounting for a linear correlation between RV and FWHM and including a quadratic background term, the noise is suppressed to the extent that a 17-d peak can be seen.

model is entirely linear, so that the vector of predicted RVs **y** can be calculated as a product of a design matrix

$$\mathbf{A_P} = \begin{pmatrix} x_0^2 & x_0 & \delta_0 & \neg\delta_0 & w_0 & \sin\left(\frac{2\pi}{P}t_0\right) & \cos\left(\frac{2\pi}{P}t_0\right) \\ \vdots & \vdots & \vdots & \vdots & \vdots & \vdots & \vdots \\ x_n^2 & x_n & \delta_n & \neg\delta_n & w_n & \sin\left(\frac{2\pi}{P}t_n\right) & \cos\left(\frac{2\pi}{P}t_n\right) \end{pmatrix}$$

(5)

and a variable vector

$$\Theta = [a, b, c_1, c_2, d, K, H]^T.$$

(6)

At the period P_b, then, the optimal parameters $\Theta_\mathbf{P}^*$ can be analytically determined as the following:

$$\Theta_\mathbf{P}^* = (\mathbf{A_P^T C^{-1} A_P})^{-1} \mathbf{A_P^T C^{-1} y},$$

(7)

where $\mathbf{C}^{-1}$ is the covariance matrix for the data, here assumed to be diagonal. We stepped through a log-uniform grid of periods between 1 and 1000 d and determine the maximum likelihood for each period (neglecting a constant term):

$$\ln\mathcal{L}_\mathbf{P}^* \sim -\frac{1}{2}(\mathbf{y} - \mathbf{A_P}\Theta_\mathbf{P}^*)^T \mathbf{C}^{-1}(\mathbf{y} - \mathbf{A_P}\Theta_\mathbf{P}^*).$$

(8)

The resulting log-likelihood periodogram shares the fundamental assumption of a circular orbit but is otherwise more robust to stellar activity and long-period trends than a traditional Lomb-Scargle periodogram (Lomb 1976; Scargle 1982). Due to the linearity of the model and the resulting ability to find the optimal parameters analytically, the likelihood may be maximized quickly and with a guarantee of convexity. Therefore, while more advanced tools exist to incorporate Bayesian priors (Olspert et al. 2018) or non-parametric correlated noise (Feng, Tuomi & Jones 2017) along with trends in the data, this method is relatively simple to implement, flexible, and fast, making it a practical solution for RV planet searches carried out in the presence of non-negligible stellar noise. The log-likelihood periodogram does show a strong peak at 17 d (Fig. 8). We show the resulting fit in Fig. 9. While this supports the presence of a sinusoidal, potentially Keplerian signal in the data, we note that this conclusion depends on the noise model adopted. The 17-d peak is the highest in the log-likelihood periodogram, but
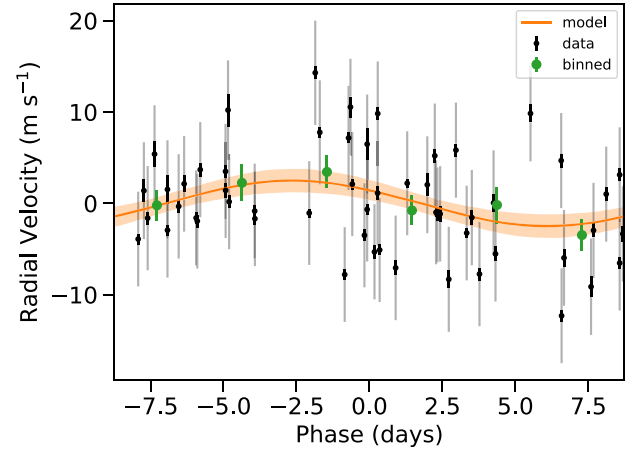

Figure 9. Phase-folded radial velocities for HD 183579b using the BM+FWHM fit. Individual data points and their photon-noise-based uncertainties are shown as black points and error bars, while the grey error bars represent the uncertainties inflated by the best-fitting (posterior median) jitter parameters. Green points are the error-weighted means within a series of phase bins. The best-fitting BM+FWHM model is shown as a solid orange line, with the shaded region around it marking the model's 1σ credible interval.

a forest of other strong peaks remain. In brief, the above analysis shows that the RV data do support the detection of a 17-d planet, but the signal is not sufficiently strong or robust to changes in the noise model to confidently claim detection on the grounds of RVs alone.

The results of the log-likelihood periodogram experiment motivated us to include an RV-FWHM correlation term in the RV model (BM+FWHM). We implemented this model fit using `pymc3` and the `exoplanet` package (Salvatier, Wiecki & Fonnesbeck 2016; Foreman-Mackey et al. 2020). The parametrization and priors adopted were identical those used in the `juliet` analysis, with the addition of two free parameters: the slope of the linear correlation between RV and FWHM, S_{FWHM}, and an offset of the post-HARPS-upgrade FWHM measurements with respect to the pre-upgrade FWHMs, Δ_{FWHM}. Both of these parameters received broad and uninformative Gaussian priors.

Table 4. Parameters, prior settings, and the best-fitting values for the HD 183579 system of three models.

Parameter	Priors	BM for HARPS	**BM+FWHM for HARPS**	BM for HARPS+Minerva
Planetary parameters				
P_b (d)	$\mathcal{N}(17.47128, 0.00005^2)$	$17.47129^{+0.00004}_{-0.00004}$	$17.4712750^{+0.0000097}_{-0.0000153}$	$17.47128^{+0.00005}_{-0.00004}$
$T_{0,b}$ (BJD)	$\mathcal{N}(245\,8661.0628, 0.0007^2)$	$2458661.06279^{+0.00050}_{-0.00051}$	$2458661.06279^{+0.00071}_{-0.00069}$	$2458661.06279^{+0.00054}_{-0.00054}$
e_b	Fixed	0	0	0
ω_b (deg)	Fixed	90	90	90
RV offset				
$\mu_{HARPS_{pre}}$ (m s^{-1})	$\mathcal{U}(-10, 10)$	$0.64^{+0.89}_{-0.88}$	$0.9^{+0.9}_{-0.9}$	$0.65^{+0.90}_{-0.90}$
$\mu_{HARPS_{post}}$ (m s^{-1})	$\mathcal{U}(-10, 10)$	$1.28^{+1.33}_{-1.35}$	$0.7^{+6.5}_{-5.6}$	$1.30^{+1.32}_{-1.33}$
μ_{MA} (m s^{-1})	$\mathcal{U}(-20, 20)$	-	-	$6.51^{+5.31}_{-5.65}$
μ_{MB} (m s^{-1})	$\mathcal{U}(-20, 20)$	-	-	$0.95^{+4.77}_{-4.88}$
μ_{MC} (m s^{-1})	$\mathcal{U}(-20, 20)$	-	-	$-5.98^{+4.60}_{-4.60}$
μ_{MD} (m s^{-1})	$\mathcal{U}(-20, 20)$	-	-	$-2.17^{+4.83}_{-5.20}$
RV noise				
$\sigma_{HARPS_{pre}}$ (m s^{-1})	$\mathcal{U}(0, 10)$	$5.32^{+0.75}_{-0.63}$	$5.17^{+0.72}_{-0.57}$	$5.30^{+0.75}_{-0.60}$
$\sigma_{HARPS_{post}}$ (m s^{-1})	$\mathcal{U}(0, 10)$	$5.86^{+1.18}_{-0.89}$	$5.65^{+1.12}_{-0.85}$	$5.88^{+1.14}_{-0.90}$
σ_{MA} (m s^{-1})	$\mathcal{U}(0, 20)$	-	-	$9.97^{+5.33}_{-4.81}$
σ_{MB} (m s^{-1})	$\mathcal{U}(0, 20)$	-	-	$12.75^{+3.63}_{-3.45}$
σ_{MC} (m s^{-1})	$\mathcal{U}(0, 20)$	-	-	$16.85^{+1.88}_{-2.42}$
σ_{MD} (m s^{-1})	$\mathcal{U}(0, 20)$	-	-	$10.12^{+4.69}_{-3.98}$
Stellar activity				
S_{FWHM}	$\mathcal{N}(0, 10)$	-	$0.4^{+4.9}_{-4.1}$	-
Δ_{FWHM}	$\mathcal{N}(0, 5)$	-	$0.1^{+2.4}_{-2.3}$	-
RV semi-amplitude				
K_b (m s^{-1})	$\mathcal{U}(0, 10)$	$2.3^{+1.1}_{-1.0}$	$2.7^{+1.3}_{-1.3}$	$2.2^{+1.0}_{-0.9}$
Derived parameters				
$M_p^{[1]}$ ($M_\oplus$)		$9.6^{+4.5}_{-4.2}$	$11.2^{+5.4}_{-5.4}$	$9.1^{+4.2}_{-3.7}$
ρ_p (g cm^{-3})		$1.2^{+0.8}_{-0.6}$	$1.4^{+0.9}_{-0.8}$	$1.2^{+0.6}_{-0.8}$

[a]This is not a statistically significant measurement. 3σ mass upper limit is $27.4\,M_\oplus$.

We regard this BM+FWHM model as our final best model because (1) The BM+FWHM model yields constraints on the planet parameters that are in full agreement with the BM model (Fig. 9, Table 4); (2) The BM+FWHM takes stellar activity into consideration while the BM model does not. Though including the FWHM term reduces the white-noise jitter slightly, it is an insignificant reduction, which suggests that the source of the excess noise in the HARPS RV measurements is not sufficiently captured by an FWHM correlation. More RV observations taken with denser sampling to preserve coherency of the stellar activity signal may be necessary to improve the noise model.

4.2.2 Including the Minerva data

We finally re-ran a Keplerian fit after including the Minerva-Australis RVs. As HD 183579 is monitored by four telescopes (Minerva 1, 3, 4, and 5; denoted as MA, MB, MC, and MD) in the array, we treated each data set separately and fit individual offsets and jitters, but kept the same prior settings for other parameters as in Section 4.2.1. We obtained $K_b = 2.2^{+1.0}_{-0.9}$ m s^{-1}, which corresponds to a mass of $9.2^{+4.1}_{-3.7}\,M_\oplus$ with a 3σ upper limit of $21.7\,M_\oplus$, estimated using the 99.7 per cent value of K_b in the posterior distribution. This measurement is consistent with the estimate from the HARPS-only data analysis within 1σ. We list our final results in Table 4 and show the best-fitting model of all data in Fig. B1. As the Minerva data were noisy with low cadence, we did not attempt to use them to fit the stellar activity.

5 SOLAR ANALOGUES WITH PLANETS

A unique aspect of solar twin planet host stars is the ability to resolve their photospheric abundances at very high precision when compared to the Sun. The relationship between a star's composition and the nature of its planetary system is an open question (Hinkel & Unterborn 2018; Clark et al. 2021), and solar twins present a promising avenue of investigation.

The Sun has been previously found to have a depletion in refractory elements compared to the volatile elements when contrasted with the refractory-to-volatile content of most nearby solar analogues (Meléndez et al. 2009; Ramírez, Meléndez & Asplund 2009). This phenomenon is found by looking at the correlation between the abundance ratio [X/H] (or sometimes [X/Fe]) and condensation temperature T_c across multiple elements X. For the majority of stars surveyed, solar-normalized photospheric abundance [X/H] correlates positively with T_c, indicating that more refractory (higher T_c) elements are over-represented in these stars compared to the Sun. It has been suggested that the Sun's relative depletion in refractories can be attributed to terrestrial planet formation, with refractory materials in the Solar protoplanetary disc being preferentially 'locked up' in planetesimals before the disc material was accreted on to the Sun (Meléndez et al. 2009). Indeed, later work from Chambers (2010) demonstrated that the difference would disappear if adding 4 $M_\oplus$ of Earth-like material to the solar convection zone. Additionally, alternative theories including planet ingestion (Ramírez et al. 2011; Spina et al. 2015; Oh et al. 2018; Church, Mustill & Liu 2020) and
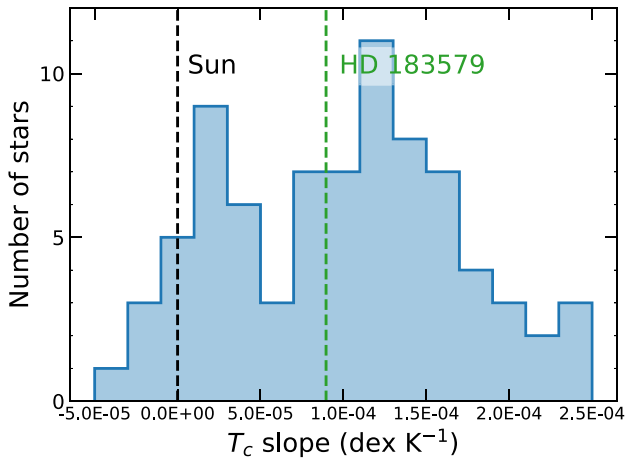
Figure 10. Histogram of abundance–condensation temperature (T_c) trends observed in a 79-star sample of solar twins studied by Bedell et al. (2018). HD 183579 is a member of this sample and its abundance pattern appears typical among solar twins. The abundance patterns for both HD 183579 and the general solar twin sample have been corrected for galactic chemical evolution effects as described in Bedell et al. (2018).

galactic chemical evolution (GCE; Adibekyan et al. 2014; Nissen 2015; Spina, Meléndez & Ramírez 2016), might be able to explain this phenomenon. However, Bedell et al. (2018) confirmed that the depletion pattern still exists even if the GCE effect has been corrected. More recently, Booth & Owen (2020) proposed that the gap opened during the giant planet formation may limit dust accretion by the host star from the disc area exterior to the forming giant planet, which may also result in the depletion in the star like our Sun.

While the exact cause of the Sun's atypical abundance pattern is still unclear, it is informative to look at HD 183579 as an example of a solar twin with a markedly different planetary system to the Sun's. Many of the HARPS spectra used in this analysis were previously used to analyse the spectroscopic properties and abundances of HD 183579 at high precision using a line-by-line differential equivalent width technique (Bedell et al. 2018; Spina et al. 2018). The abundances of 30 elements were used to examine the behaviour of abundance with T_c for 79 solar twins, including HD 183579, in Bedell et al. (2018). Using the galactic chemical evolution-corrected abundance-T_c relations measured in that work, we show that HD 183579 is a typical Sun-like star, without a statistically significant refractory element depletion (Fig. 10).

All of these motivate us to examine if the majority of solar analogues hosting rocky planets (or planets with rocky cores, such as mini-Neptunes) show similar depletion as our Sun, or significant depletion. We used the homogeneous California-Kepler Survey (CKS) catalogue to build our planet sample (Johnson et al. 2017; Petigura et al. 2017). There are a total of 1305 CKS spectra of 'Kepler Objects of Interest' (KOIs) that hosting 2025 planet candidates, which precisely measure the stellar properties. We retrieved the publicly available abundances derived by Brewer et al. (2016) and Brewer & Fischer (2018), which achieved a typical internal abundance precision at ∼0.04 dex level. We first threw out targets flagged as false positives or without dispositions in the catalog, leaving the stars with at least one or more confirmed planets/planet candidates. We then included stars with: (1) 5680 K < T_{eff} < 5880 K; (2) $\sigma_{T_{eff}}$ < 70 K; (3) 4.3 dex < log g < 4.5 dex; (4) $\sigma_{\log g}$ < 0.1 dex; (5) −0.1 dex < [Fe/H] < 0.1 dex; (6) $\sigma_{[Fe/H]}$ < 0.05 dex. We found 39 planet–host solar analogues. Since CKS only has a few known giant planet
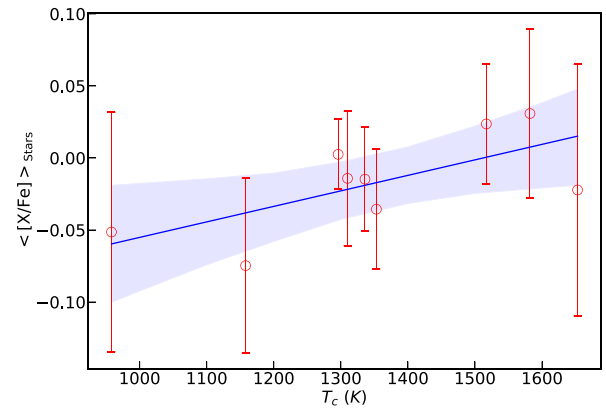

Figure 11. The mean abundance of the 36 CKS solar twin planet sample. The error bars represent the standard deviations of each elemental abundance. The blue solid line is the linear fit to the T_c trend. The shaded region represents the 1σ confidence interval.

hosts and those systems may bias our comparison as the giant planet formation is also suspected to result in the depletion phenomenon (Booth & Owen 2020), we further removed 3 systems with at least one planet with radius larger than 8$R_\oplus$ (KOI 1, KOI 372 and KOI 1089), thus our final sample contains 36 stars. We computed the mean abundance of each element (Na, Mg, Al, Si, Ca, Ti, Cr, Mn, Ni), and performed a least-squares fit to the [X/Fe] as a function of the condensation temperature T_c.[6] The result is presented in Fig. 11. We tentatively found that solar analogues with rocky planets/rocky cores (i.e. mini-Neptunes) do not show a similar depletion as our Sun. However, this preliminary result is limited by the methodology used to derive the chemical abundance. With the current small number of precisely characterized solar twins with known planets, we cannot draw any conclusions.

6 DISCUSSION

6.1 Atmospheric characterization of HD 183579b

Although thousands of large sub-Neptunes (2.75 $R_\oplus$ < R_p < 4 $R_\oplus$) have been detected up to now, only ∼40 of them are orbiting around bright stars (K < 10 mag). With K = 7.15 mag, HD 183579b is hosted by the fifth brightest star among them (HD 21749b, Dragomir et al. 2019; Trifonov, Rybizki & Kürster 2019; Gan et al. 2021; GJ 436b, Butler et al. 2004; Knutson et al. 2011; HD 95338b, Díaz et al. 2020; and HD 3167c, Vanderburg et al. 2016; Livingston et al. 2018), making it an excellent target for future atmospheric characterization using the upcoming *James Webb Space Telescope* (*JWST*, Gardner et al. 2006) and *Extremely Large Telescope* (*ELT*, Gilmozzi & Spyromilio 2007; de Zeeuw, Tamai & Liske 2014).

Following the approach in Gillon et al. (2016), we estimated the signal amplitude of HD 183579b in the transit transmission spectroscopy:

$$\text{Amp} = \frac{2R_p h_{eff}}{R_*^2}, \quad (9)$$

where R_p and R_* are the planet and stellar radius, and $h_{eff} = 7kT/\mu g$ represents the effective atmospheric height. We adopted the typical atmospheric mean molecular mass μ to be 2.3 amu for sub-Neptune

---

[6]We take the 50 per cent condensation temperatures from Lodders (2003).

planets (Demory et al. 2020). Assuming the atmospheric temperature T to be the equilibrium temperature T_{eq}, we obtained an amplitude of 243^{+164}_{-75} ppm[7] of HD 183579b, which is above the noise floor level 50 ppm of *JWST* for MIRI LRS ($\lambda = 5.0$–$11\,\mu$m) observations (Greene et al. 2016).

We further computed the Transmission Spectroscopy Metric (TSM; Kempton et al. 2018) of HD 183579b to be 126^{+168}_{-54}. Kempton et al. (2018) recommended that planets with TSM > 90 and $1.5 < R_p < 10\,R_\oplus$ are high-quality atmospheric characterization targets. Combined with the two aspects above, we regarded HD 183579b as an attractive source for further atmosphere composition analysis.

6.2 Prospects on future follow-up observations

Since the current RV data sets only enable a $\sim 2\sigma$ mass constraint, here we suggest that future RVs measurements of HD 183579 are needed to break the degeneracy between the planet mass M_p and the mean molecular weight μ (Seager & Sasselov 2000; Seager, Deming & Valenti 2009) in any atmospheric characterization studies. Additional RVs would also be crucial to search for outer long-period non-transiting cold giants (see the next subsection).

Given the brightness of HD 183579 ($V = 8.7$ mag), most high-resolution optical spectroscopy facilities like the Planet Finder Spectrograph (PFS; Crane, Shectman & Butler 2006; Crane et al. 2008, 2010) can achieve high SNR and reach the 1 m s^{-1} precision. In addition, the expected rotation time-scale of HD 183579 is well separated from the planet orbital period, making it possible to smooth out the stellar activity effects in RVs with high-cadence observations (López-Morales et al. 2016; Gan et al. 2021).

6.3 Additional planet in the HD 183579 system?

Zhu & Wu (2018) suggested a higher probability of detecting cold Jupiters around the hosts of small planets (planets with mass/radius between Earth and Neptune) compared with other field stars, which is also supported by the recent observational results from Bryan et al. (2019). As we have a long time baseline of HARPS observations (~ 3000 d), we first looked for possible periodic signals on the residuals after subtracting the best-fitting model for HD 183579b using GLS. However, we did not identify any significant peaks between 100 d and 1500 d with FAP<0.1 per cent. We then ran another BM+1pl fit to blindly search the potential cold giant planets with period between the aforementioned range. We fit the Keplerian signals of HD 183579b and another potential outer cold planet simultaneously. By adopting the same prior settings for other parameters as the BM+1pl model in Section 4.2, we obtained $\Delta \ln Z = \ln Z_{BM + 1pl} - \ln Z_{BM} = 3$, which ruled out the existence of an outer gas giant planet with mass down to Saturn mass and period up to roughly 4 yr based on the current data.

6.4 Comparison with Palatnick et al. 2021

We note that during the writing of this manuscript, Palatnick et al. (2021) validated this system using *TESS* and HARPS archival-only data (56 in total). The RV semi-amplitude of HD 183579 reported by Palatnick et al. (2021) is $4.9^{+0.9}_{-1.0}$ m s^{-1}, which is about 1.7σ larger than our measurement $2.7^{+1.3}_{-1.3}$ m s^{-1}. The discrepancy is caused by the contribution from the three recent, additional HARPS RV points taken between 2019 August 16 and 20 in this work. All of the three
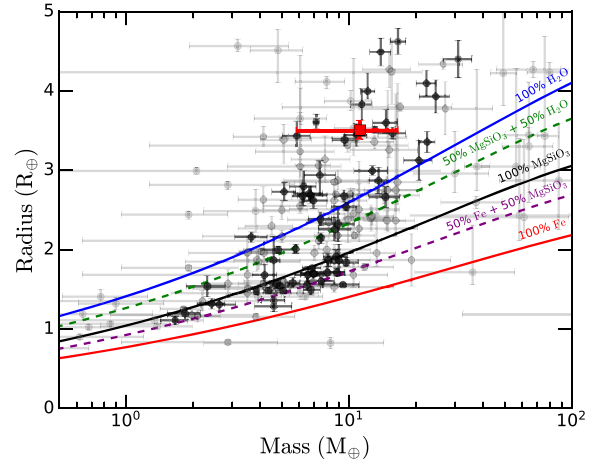
---

[7]The large error bar mainly comes from the uncertainty of the planet mass M_p.

Figure 12. The mass–radius diagram in Earth units. HD 183579b is marked as a red square. The confirmed planets with well-measured radius and mass are shown as black points (uncertainty smaller than 20 per cent) while grey points represent the planet with poor constraint (data are retrieved from NASA Exoplanet Archive; Akeson et al. 2013). The coloured lines are the theoretical *M*–*R* models for different planetary compositions, taken from Zeng & Sasselov (2013).

newly acquired HARPS spectra have high SNR (105.9, 110.3, and 95.6, respectively). Without including these HARPS RV data, as in Palatnick et al. (2021), we derived a similar RV semi-amplitude of $K_b = 5.2^{+1.1}_{-1.2}$ m s^{-1} by fitting a Keplerian model plus a linear RV slope $\dot{\gamma}$ using the same prior settings described in Section 4.2.[8] The best-fitting $\dot{\gamma}$ is $-3.3^{+0.9}_{-0.9}$ m s^{-1}yr^{-1}, consistent with the posterior value of $-3.2^{+0.8}_{-0.7}$ m s^{-1}yr^{-1} reported in Palatnick et al. (2021). However, after including the three recent HARPS RV points,[9] we found the model prefers a null RV slope ($\dot{\gamma} = -0.1^{+0.6}_{-0.8}$ m s^{-1}yr^{-1}) and the RV semi-amplitude decreases to $K_b = 2.3^{+1.2}_{-1.2}$ m s^{-1}. We show both models in Figs C1 and C2. This difference is reasonable since the stellar activity plays a role in the Doppler signals, as stated in Section 3.2, which biases the result of Palatnick et al. (2021). Thus a Keplerian+RV slope model may not be able to explain the total HARPS data set. We emphasize here that our results are still consistent within 1.7σ, and more RV data are needed to deal with the stellar activity and measure the mass of the planet more accurately.

7 SUMMARY AND CONCLUSIONS

In this paper, we characterize the HD 183579 planetary system using both space and ground-based photometric data from *TESS* and LCO as well as the spectroscopic data from HARPS and MINERVA-Australis. Our models reveal that HD 183579b is a warm sub-Neptune hosted by a nearby solar twin with an orbital period of 17.47 d, a radius of $3.53^{+0.13}_{-0.11}\,R_\oplus$ and a mass of $11.2^{+5.4}_{-5.4}\,M_\oplus$, with a 3σ upper limit of $27.4\,M_\oplus$ (see Fig. 12). Taken together, the resulting planetary bulk density of $1.4^{+0.9}_{-0.8}$ g cm^{-3}, implies that an extended atmosphere is likely present, making this system an excellent candidate for transmission spectroscopic follow-up. The line-by-line differential spectroscopic analysis shows that HD

---

[8]For the RV slope term, we adopted a uniform prior with an initial guess of 0 m s^{-1}d^{-1}.

[9]We removed one archival HARPS measurement whose BIS and FWHM were outliers (see Section 2.3.1 for more detail) so the final RV data number used in this model is 58.

183579 does not show a similar depletion in the abundance of refractory elements as our Sun. The lack of a Solar refractory depletion could plausibly be linked to HD 183579's lack of known giant planets (following the gap-opening hypothesis) or a history of planetary migration and stellar infall, especially if the planet reported here did not form *in situ* (following the planet accretion hypothesis).

ACKNOWLEDGEMENTS

DATA AVAILABILITY

This paper includes photometric data collected by the *TESS* mission and LCOGT, which is publicly available in ExoFOP, at https://exofop.ipac.caltech.edu/tess/target.php?id=320004517. All spectroscopy data underlying this article are listed in the appendix. The data will also be shared on reasonable request to the corresponding author.

REFERENCES

Addison B. et al., 2019, PASP, 131, 115003
Addison B. C. et al., 2020, preprint (arXiv:2006.13675)
Addison B. C. et al., 2021, MNRAS, 502, 3704
Adibekyan V. Z., González Hernández J. I., Delgado Mena E., Sousa S. G., Santos N. C., Israelian G., Figueira P., Bertran de Lis S., 2014, A&A, 564, L15
Akeson R. L. et al., 2013, PASP, 125, 989
Aller A., Lillo-Box J., Jones D., Miranda L. F., Barceló Forteza S., 2020, A&A, 635, A128
Angus R., Foreman-Mackey D., Johnson J. A., 2016, ApJ, 818, 109
Astropy Collaboration, 2013, A&A, 558, A33
Astropy Collaboration, 2018, AJ, 156, 123
Baglin A., Auvergne M., Barge P., Deleuil M., Catala C., Michel E., Weiss W., COROT Team, 2006, in Fridlund M., Baglin A., Lochard J., Conroy L., eds, ESA SP-1306: The CoRoT Mission Pre-Launch Status - Stellar Seismology and Planet Finding. ESA, Noordwijk, p. 33
Bakos G., Noyes R. W., Kovács G., Stanek K. Z., Sasselov D. D., Domsa I., 2004, PASP, 116, 266
Barentsen G. et al., 2019, Keplergo/lightkurve: Lightkurve v1.0b29, doi:10.5281/zenodo.2565212
Barnes S. A., 2007, ApJ, 669, 1167
Barnes S. I., Gibson S., Nield K., Cochrane D., 2012, in McLean I. S., Ramsay S. K., Takami H., eds, Proc. SPIE Conf. Ser. Vol. 8446, Ground-based and Airborne Instrumentation for Astronomy IV. SPIE, Bellingham, p. 844688
Bedell M. et al., 2015, A&A, 581, A34
Bedell M. et al., 2018, ApJ, 865, 68
Bensby T., Feltzing S., Lundström I., 2003, A&A, 410, 527
Bensby T., Feltzing S., Oey M. S., 2014, A&A, 562, A71
Booth R. A., Owen J. E., 2020, MNRAS, 493, 5079
Borucki W. J. et al., 2010, Science, 327, 977
Bovy J., 2015, ApJS, 216, 29
Brewer J. M., Fischer D. A., 2018, ApJS, 237, 38
Brewer J. M., Fischer D. A., Valenti J. A., Piskunov N., 2016, ApJS, 225, 32
Brown T. M., 2003, ApJ, 593, L125
Brown T. M. et al., 2013, PASP, 125, 1031
Bryan M. L., Knutson H. A., Lee E. J., Fulton B. J., Batygin K., Ngo H., Meshkat T., 2019, AJ, 157, 52
Butler R. P., Vogt S. S., Marcy G. W., Fischer D. A., Wright J. T., Henry G. W., Laughlin G., Lissauer J. J., 2004, ApJ, 617, 580
Chambers J. E., 2010, ApJ, 724, 92
Chazelas B. et al., 2012, in Stepp L. M., Gilmozzi R., Hall H. J., Proc. SPIE Conf. Ser. Vol. 8444, Ground-based and Airborne Telescopes IV. SPIE, Bellingham, p. 84440E
Chen J., Kipping D., 2017, ApJ, 834, 17
Church R. P., Mustill A. J., Liu F., 2020, MNRAS, 491, 2391
Clark J. T. et al., 2021, MNRAS, 504, 4968
Collins K. A., Kielkopf J. F., Stassun K. G., Hessman F. V., 2017, AJ, 153, 77

Crane J. D., Shectman S. A., Butler R. P., 2006, in McLean Ian S., Iye Masanori, eds, Proc. SPIE Conf. Ser. Vol. 6269, The Carnegie Planet Finder Spectrograph. SPIE, Bellingham, p. 626931

Crane J. D., Shectman S. A., Butler R. P., Thompson I. B., Burley G. S., 2008, in McLean Ian S., Casali Mark M., eds, Proc. SPIE Conf. Ser. Vol. 7014, The Carnegie Planet Finder Spectrograph: a Status Report. SPIE, Bellingham, p. 701479

Crane J. D., Shectman S. A., Butler R. P., Thompson I. B., Birk C., Jones P., Burley G. S., 2010, in McLean I. S., Ramsay S. K., Takami H., eds, Proc. SPIE Conf. Ser. Vol. 7735, The Carnegie Planet Finder Spectrograph: Integration and Commissioning. SPIE, Bellingham, p. 773553

Curtis J. L. et al., 2018, AJ, 155, 173

Curtis J. L., Agüeros M. A., Douglas S. T., Meibom S., 2019, ApJ, 879, 49

Cutri R. M. et al., 2003, 2MASS All Sky Catalog of Point Sources. VizieR Online Data Catalog, II/246

de Zeeuw T., Tamai R., Liske J., 2014, The Messenger, 158, 3

Demory B. O. et al., 2020, A&A, 642, A49

Díaz M. R. et al., 2020, MNRAS, 496, 4330

Dragomir D. et al., 2019, ApJ, 875, L7

Espinoza N., 2018, Res. Notes Am. Astron. Soc., 2, 209

Espinoza N., Kossakowski D., Brahm R., 2019, MNRAS, 490, 2262

Feng F., Tuomi M., Jones H. R. A., 2017, MNRAS, 470, 4794

Foreman-Mackey D., Agol E., Ambikasaran S., Angus R., 2017, AJ, 154, 220

Foreman-Mackey D., Luger R., Czekala I., Agol E., Price-Whelan A., Barclay T., 2020, exoplanet-dev/exoplanet v0.3.2, doi:10.5281/zenodo.1998447

Fulton B. J., Petigura E. A., Blunt S., Sinukoff E., 2018, PASP, 130, 044504

Gaia Collaboration, 2018, A&A, 616, A1

Gaia Collaboration, 2021, A&A, 649, A1

Gan T. et al., 2020, AJ, 159, 160

Gan T. et al., 2021, MNRAS, 501, 6042

Gardner J. P. et al., 2006, Space Sci. Rev., 123, 485

Gillon M. et al., 2016, Nature, 533, 221

Gilmozzi R., Spyromilio J., 2007, The Messenger, 127, 11

Greene T. P., Line M. R., Montero C., Fortney J. J., Lustig-Yaeger J., Luther K., 2016, ApJ, 817, 17

Higson E., Handley W., Hobson M., Lasenby A., 2019, Stat. Comput., 29, 891

Hinkel N. R., Unterborn C. T., 2018, ApJ, 853, 83

Hirano T. et al., 2018, AJ, 155, 124

Horner J. et al., 2020, PASP, 132, 102001

Howell S. B., Everett M. E., Sherry W., Horch E., Ciardi D. R., 2011, AJ, 142, 19

Howell S. B. et al., 2014, PASP, 126, 398

Huang C. X. et al., 2018, preprint (arXiv:1807.11129)

Husser T.-O., Wende-von Berg S., Dreizler S., Homeier D., Reiners A., Barman T., Hauschildt P. H., 2013, A&A, 553, A6

Høg E. et al., 2000, A&A, 355, L27

Jenkins J. M., 2002, ApJ, 575, 493

Jenkins J. M. et al., 2016, Software and Cyberinfrastructure for Astronomy IV. Vol. 9913, The TESS science processing operations center, SPIE, p. 99133E

Jenkins J. M., Tenenbaum P., Seader S., Burke C. J., McCauliff S. D., Smith J. C., Twicken J. D., Chandrasekaran H., 2017, Technical report, Kepler Data Processing Handbook: Transiting Planet Search.

Jensen E., 2013, Tapir: A web interface for transit/eclipse observability, record ascl:1306.007

Johnson D. R. H., Soderblom D. R., 1987, AJ, 93, 864

Johnson J. A. et al., 2017, AJ, 154, 108

Jordán A. et al., 2020, AJ, 159, 145

Kane S. R. et al., 2021, J. Geophys. Res., 126, e06643

Kempton E. M.-R. et al., 2018, PASP, 130, 114401

Kipping D. M., 2013, MNRAS, 435, 2152

Knutson H. A. et al., 2011, ApJ, 735, 27

Kovács G., Zucker S., Mazeh T., 2002, A&A, 391, 369

Kreidberg L., 2015, PASP, 127, 1161

Labadie-Bartz J. et al., 2019, ApJS, 240, 13

Li J., Tenenbaum P., Twicken J. D., Burke C. J., Jenkins J. M., Quintana E. V., Rowe J. F., Seader S. E., 2019, PASP, 131, 024506

Lightkurve Collaboration, 2018, Lightkurve: Kepler and TESS time series analysis in Python, record ascl:1812.013

Lissauer J. J. et al., 2011, Nature, 470, 53

Livingston J. H. et al., 2018, AJ, 156, 277

Lo Curto G. et al., 2015, The Messenger, 162, 9

Lodders K., 2003, ApJ, 591, 1220

Lomb N. R., 1976, Ap&SS, 39, 447

López-Morales M. et al., 2016, AJ, 152, 204

Lorenzo-Oliveira D. et al., 2018, A&A, 619, A73

Lovis C. et al., 2011, preprint (arXiv:1107.5325)

McCully C., Volgenau N. H., Harbeck D.-R., Lister T. A., Saunders E. S., Turner M. L., Siiverd R. J., Bowman M., 2018, Software and Cyberinfrastructure for Astronomy V. SPIE, p. 107070K

McQuillan A., Mazeh T., Aigrain S., 2014, ApJS, 211, 24

Mamajek E. E., Hillenbrand L. A., 2008, ApJ, 687, 1264

Mayor M., Queloz D., 1995, Nature, 378, 355

Mayor M. et al., 2003, The Messenger, 114, 20

Meibom S., Mathieu R. D., Stassun K. G., 2009, ApJ, 695, 679

Meléndez J., Asplund M., Gustafsson B., Yong D., 2009, ApJ, 704, L66

Meléndez J. et al., 2015, The Messenger, 161, 28

Morrissey P. et al., 2007, ApJS, 173, 682

Mortier A., Faria J. P., Correia C. M., Santerne A., Santos N. C., 2015, A&A, 573, A101

Nissen P. E., 2015, A&A, 579, A52

Oh S., Price-Whelan A. M., Brewer J. M., Hogg D. W., Spergel D. N., Myles J., 2018, ApJ, 854, 138

Olspert N., Pelt J., Käpylä M. J., Lehtinen J., 2018, A&A, 615, A111

Palatnick S., Kipping D., Yahalomi D., 2021, ApJ, 909, L6

Parviainen H., Aigrain S., 2015, MNRAS, 453, 3821

Paunzen E., 2015, A&A, 580, A23

Pepe F., Mayor M., Galland F., Naef D., Queloz D., Santos N. C., Udry S., Burnet M., 2002, A&A, 388, 632

Pepper J. et al., 2007, PASP, 119, 923

Pepper J., Kuhn R. B., Siverd R., James D., Stassun K., 2012, PASP, 124, 230

Petigura E. A. et al., 2017, AJ, 154, 107

Pollacco D. L. et al., 2006, PASP, 118, 1407

Ramírez I., Meléndez J., Asplund M., 2009, A&A, 508, L17

Ramírez I., Meléndez J., Cornejo D., Roederer I. U., Fish J. R., 2011, ApJ, 740, 76

Ramírez I. et al., 2014, A&A, 572, A48

Ricker G. R. et al., 2014, in Oschmann J., Jacobus M., Clampin M., Fazio G. G., MacEwen H. A., eds, Space Telescopes and Instrumentation 2014: Optical, Infrared, and Millimeter Wave. Vol. 9143, SPIE, p. 914320

Ricker G. R. et al., 2015, J. Astron. Telescopes Instrum. Syst., 1, 014003

Salvatier J., Wiecki T. V., Fonnesbeck C., 2016, PeerJ Comput. Sci., 2, e55

Scargle J. D., 1982, ApJ, 263, 835

Schlegel D. J., Finkbeiner D. P., Davis M., 1998, ApJ, 500, 525

Seager S., Sasselov D. D., 2000, ApJ, 537, 916

Seager S., Deming D., Valenti J. A., 2009, Astrophys. Space Sci. Proc., 10, 123

Skrutskie M. F. et al., 2006, AJ, 131, 1163

Smith J. C. et al., 2012, PASP, 124, 1000

Soto M. G., Jenkins J. S., 2018, A&A, 615, A76

Speagle J. S., 2020, MNRAS, 493, 3132

Spina L. et al., 2015, A&A, 582, L6

Spina L., Meléndez J., Ramírez I., 2016, A&A, 585, A152

Spina L. et al., 2018, MNRAS, 474, 2580

Stassun K. G., Torres G., 2016, AJ, 152, 180

Stassun K. G., Collins K. A., Gaudi B. S., 2017, AJ, 153, 136

Stassun K. G., Corsaro E., Pepper J. A., Gaudi B. S., 2018a, AJ, 155, 22

Stassun K. G. et al., 2018b, AJ, 156, 102

Stassun K. G. et al., 2019, AJ, 158, 138

Stumpe M. C. et al., 2012, PASP, 124, 985
Stumpe M. C., Smith J. C., Catanzarite J. H., Van Cleve J. E., Jenkins J. M., Twicken J. D., Girouard F. R., 2014, PASP, 126, 100
Sullivan P. W. et al., 2015, ApJ, 809, 77
Theano Development Team, 2016, preprint (abs/1605.02688)
Tokovinin A., 2018, PASP, 130, 035002
Torres G., Andersen J., Giménez A., 2010, A&AR, 18, 67
Trifonov T., Rybizki J., Kürster M., 2019, A&A, 622, L7
Trotta R., 2008, Contemp. Phys., 49, 71
Twicken J. D. et al., 2018, PASP, 130, 064502
Vanderburg A. et al., 2016, ApJ, 829, L9

Wheatley P. J. et al., 2018, MNRAS, 475, 4476
Wright E. L. et al., 2010, AJ, 140, 1868
Wright J. T., Eastman J. D., 2014, PASP, 126, 838
Yana Galarza J., Meléndez J., Ramírez I., Yong D., Karakas A. I., Asplund M., Liu F., 2016, A&A, 589, A17
Yee S. W., Petigura E. A., von Braun K., 2017, ApJ, 836, 77
Zechmeister M. et al., 2018, A&A, 609, A12
Zeng L., Sasselov D., 2013, PASP, 125, 227
Zhu W., Wu Y., 2018, AJ, 156, 92
Ziegler C., Tokovinin A., Briceño C., Mang J., Law N., Mann A. W., 2020, AJ, 159, 19

APPENDIX A: ALL RVS AND STELLAR ACTIVITY INDICATORS OF HARPS AND MINERVA-AUSTRALIS

Table A1. HARPS RVs and stellar activity indicators.

Time (BJD)	RV (m s^{-1})	RVerr (m s^{-1})	CRX	CRXerr	DLW	DLWerr	BIS	FWHM	S_{HK}	S_{HK}err
2455847.536	14.37	1.53	− 1.16	12.18	1.99	2.49	− 0.025	7.091	0.1821	0.0014
2455850.515	2.02	0.82	− 10.75	6.45	− 1.97	1.27	− 0.016	7.079	0.191	0.0008
2455851.518	− 0.3	0.71	1.63	5.75	− 7.83	1.18	− 0.015	7.068	0.1901	0.0007
2455852.505	− 1.39	1.22	3.17	9.84	− 10.34	1.64	− 0.019	7.062	0.1897	0.0009
2456042.793	4.35	1.15	11.92	9.15	− 10.75	1.47	− 0.024	7.073	0.1852	0.001
2456043.878	3.59	1.21	− 3.85	9.74	− 8.64	1.55	− 0.019	7.074	0.1854	0.001
2456045.888	15.57	1.37	− 25.38	10.55	− 2.59	2.25	− 0.018	7.078	0.1894	0.0012
2456046.939	10.58	0.86	− 17.16	6.6	7.91	1.27	− 0.017	7.082	0.1909	0.0009
2456048.942	7.96	0.97	− 8.24	7.75	19.62	1.82	− 0.015	7.075	0.1944	0.0009
2456162.592	10.61	2.11	− 14.78	16.61	6.19	3.48	− 0.014	7.087	0.1872	0.0018
2456164.651	7.01	1.49	− 10.12	11.79	− 2.52	2.14	− 0.017	7.082	0.1972	0.0015
2456165.633	9.13	1.01	− 8.8	8.1	− 1.67	1.44	− 0.019	7.072	0.1965	0.0009
2456378.907	− 7.67	0.82	14.47	6.39	− 0.23	1.1	− 0.019	7.073	0.1892	0.0008
2456484.744	− 3.47	1.81	35.43	13.85	− 0.01	2.17	− 0.026	7.09	0.1769	0.0014
2456485.724	− 2.08	1.03	19.75	7.82	− 3.14	1.34	− 0.021	7.081	0.1912	0.0008
2456486.702	1.27	0.93	23.83	6.83	0.36	0.89	− 0.024	7.084	0.1945	0.0007
2456487.706	2.01	0.96	27.73	6.86	− 0.97	0.93	− 0.022	7.081	0.195	0.0007
2456488.727	3.66	0.98	29.05	6.91	2.78	1.23	− 0.022	7.087	0.1939	0.0009
2456489.694	7.93	0.99	− 12.21	7.79	5.59	1.36	− 0.011	7.09	0.1934	0.0009
2456490.7	1.49	0.92	− 16.04	7.1	2.04	1.19	− 0.018	7.081	0.1928	0.0008
2456557.59	6.92	1.65	12.62	12.95	4.51	3.16	− 0.017	7.087	0.1926	0.0018
2456558.572	3.15	0.98	2.53	7.89	− 0.06	1.18	− 0.02	7.073	0.191	0.0008
2456559.583	7.07	1.06	− 11.08	8.36	− 2.82	1.43	− 0.02	7.077	0.1885	0.001
2456560.578	3.09	0.83	− 13.03	6.48	0.53	1.15	− 0.023	7.071	0.189	0.0008
2456850.714	− 0.38	1.23	− 6.28	9.74	6.38	1.74	− 0.017	7.072	0.1932	0.0012
2456851.725	2.3	1.04	− 7.54	8.29	5.97	1.36	− 0.016	7.076	0.1869	0.001
2456852.73	1.74	1.07	− 19.51	8.19	− 1.3	1.71	− 0.021	7.075	0.1939	0.001
2456853.794	9.94	1.93	− 6.63	15.39	5.63	2.25	− 0.018	7.088	0.173	0.0014
2456855.725	8.36	1.11	− 17.74	8.68	1.32	1.45	− 0.02	7.083	0.1916	0.0009
2456856.715	4.03	0.83	− 13.81	6.47	3.66	1.27	− 0.015	7.084	0.1947	0.0009
2456904.574	5.07	0.92	− 21.63	6.78	− 1.63	1.28	− 0.023	7.074	0.1872	0.0009
2456906.573	5.58	1.58	6.81	12.49	1.74	2.79	− 0.018	7.079	0.1792	0.0015
2456907.587	4.38	1.24	− 13.04	9.71	1.04	1.76	− 0.022	7.076	0.194	0.0012
2456961.505	11.57	2.43	− 7.7	19.4	5.59	3.13	− 0.028	7.083	0.1818	0.0019
2456965.501	− 3.57	0.75	1.78	6.02	− 0.66	0.97	− 0.021	7.082	0.1885	0.0007
2456966.521	− 1.39	1.01	0.58	8.2	− 2.71	1.35	− 0.023	7.079	0.1893	0.0009
2457226.716	10.4	0.96	− 3.69	7.98	4.29	1.1	− 0.004	7.1	0.1934	0.0007
2457227.703	10.21	1.11	− 4.51	9.22	4.28	0.9	− 0.007	7.104	0.1953	0.0007
2457228.698	4.03	1.22	− 6.97	10.15	4.88	1.3	− 0.004	7.104	0.196	0.001
2457229.711	4.87	1.07	0.36	9.06	4.28	0.79	− 0.004	7.1	0.1927	0.0006
2457230.698	1.2	0.92	1.46	7.79	2.64	0.83	− 0.004	7.095	0.1891	0.0006

Table A1 – *continued*

Time (BJD)	RV (m s^{-1})	RVerr (m s^{-1})	CRX	CRXerr	DLW	DLWerr	BIS	FWHM	S_{HK}	S_{HK}err
2457232.67	1.54	1.52	− 7.21	12.74	3.76	1.83	− 0.002	7.104	0.1861	0.0012
2457283.549	− 6.69	1.56	0.72	12.94	− 5.74	2.0	− 0.004	7.088	0.1875	0.0011
2457284.601	− 5.29	1.05	7.82	8.72	− 2.45	1.1	− 0.009	7.09	0.1889	0.0008
2457507.88	2.41	1.5	− 1.29	12.65	7.57	1.16	− 0.004	7.117	0.1824	0.0006
2457587.718	1.44	1.06	4.99	8.79	− 4.88	1.24	− 0.007	7.087	0.1807	0.0008
2457588.767	1.86	1.02	− 9.51	8.38	− 5.32	0.91	0.036	7.139	0.1791	0.0008
2457588.78	2.33	1.08	0.07	8.89	− 4.64	1.46	− 0.012	7.082	0.1797	0.0009
2457664.611	3.37	0.96	− 9.33	7.8	− 5.5	0.97	− 0.005	7.095	0.1857	0.0008
2457665.549	− 2.78	1.04	9.86	8.57	− 3.84	1.14	− 0.006	7.096	0.184	0.0008
2457682.499	− 1.45	0.85	9.3	6.97	− 3.19	1.08	− 0.013	7.09	0.186	0.0007
2457683.568	− 3.81	0.97	3.03	8.04	− 7.46	1.26	− 0.018	7.088	0.1875	0.001
2458047.504	0.16	0.98	− 2.6	8.15	− 3.8	0.67	− 0.009	7.088	0.184	0.0006
2458711.619	15.76	1.18	4.2	9.88	2.83	1.19	− 0.008	7.1	0.204	0.0008
2458713.76	13.1	1.14	9.7	9.52	5.74	1.38	− 0.006	7.102	0.1998	0.001
2458715.714	8.67	1.08	− 10.43	9.04	2.9	1.14	− 0.009	7.103	0.2021	0.0009

Table A2. MINERVA-Australis RVs of 4 telescopes: MA, MB, MC and MD.

Time(BJD)	RV(m s^{-1})	RVerr(m s^{-1})	Instrument
245 8961.205	13.51	8.03	MA
245 8964.276	− 5.64	8.17	MA
245 8966.254	0.3	8.35	MA
245 8980.084	− 6.58	8.67	MA
245 8981.194	20.78	7.4	MA
245 8959.285	− 17.62	5.0	MB
245 8961.205	11.8	6.36	MB
245 8964.276	− 4.74	5.22	MB
245 8966.254	− 1.2	5.29	MB
245 8971.214	1.2	8.62	MB
245 8971.236	− 17.36	8.93	MB
245 8973.184	19.1	5.2	MB
245 8973.206	13.31	5.17	MB
245 8959.285	− 34.61	6.39	MC
245 8961.205	− 14.81	7.23	MC
245 8964.276	− 28.45	6.54	MC
245 8966.254	− 41.26	6.91	MC
245 8973.184	8.17	6.09	MC
245 8973.206	9.67	6.35	MC
245 8974.308	1.66	7.46	MC
245 8980.084	− 0.27	8.1	MC
245 8980.106	20.03	8.04	MC
245 8981.172	7.12	6.76	MC
245 8981.194	14.62	6.66	MC
245 8995.32	− 31.32	8.98	MC
245 8998.047	− 11.82	6.91	MC
245 8998.069	9.99	6.86	MC
245 9002.078	− 13.7	7.22	MC
245 8995.32	− 20.95	5.55	MD
245 8998.047	6.44	6.23	MD
245 8998.069	0.0	5.57	MD
245 9002.078	− 3.96	5.75	MD
245 9002.099	3.82	7.18	MD

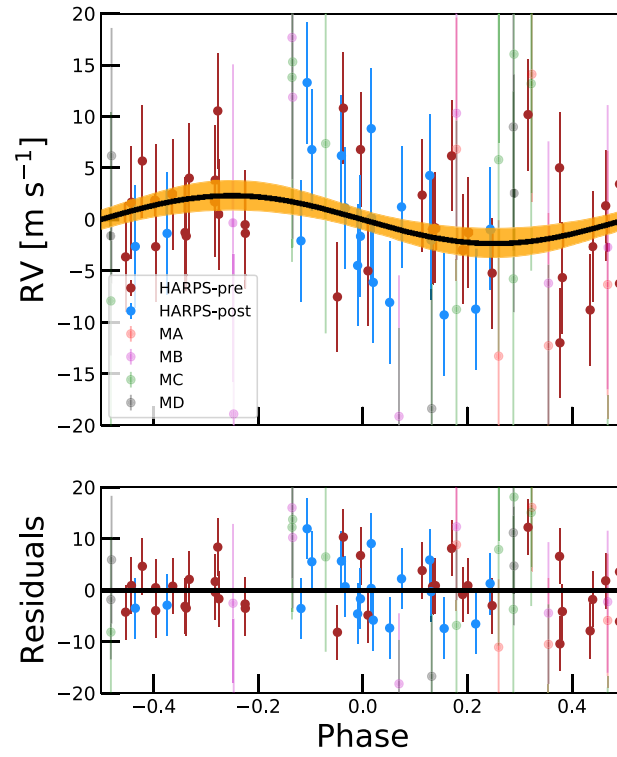## APPENDIX B: BM FOR HARPS AND MINERVA

Figure B1. The phase-folded HARPS and MINERVA RVs of HD 183579. The best-fitting base model is shown as a black solid line. The orange shaded region represents the 1σ confidence interval of the model. Residuals are plotted below.

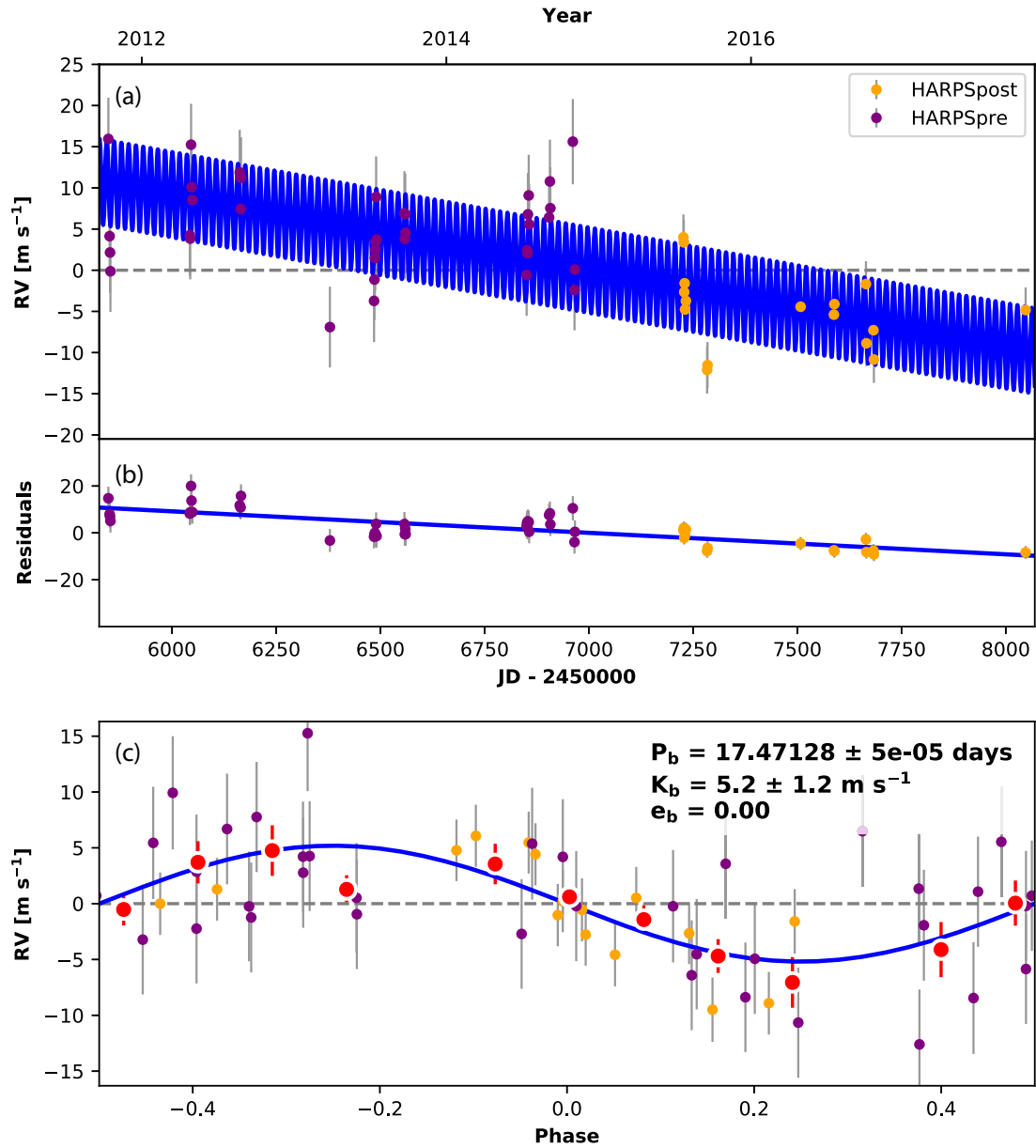## APPENDIX C: MODEL COMPARISON

Figure C1. HARPS archive-only data used in Palatnick et al. (2021) and the best-fitting model. The top panel shows the full RV time series and residuals. The phase-folded RV data are presented in the bottom panel. The red points are the binned RVs.

Figure C2. HARPS archive-only data plus three additional RV points along with the best-fitting model. The top panel shows the full RV time series and residuals. The phase-folded RV data are presen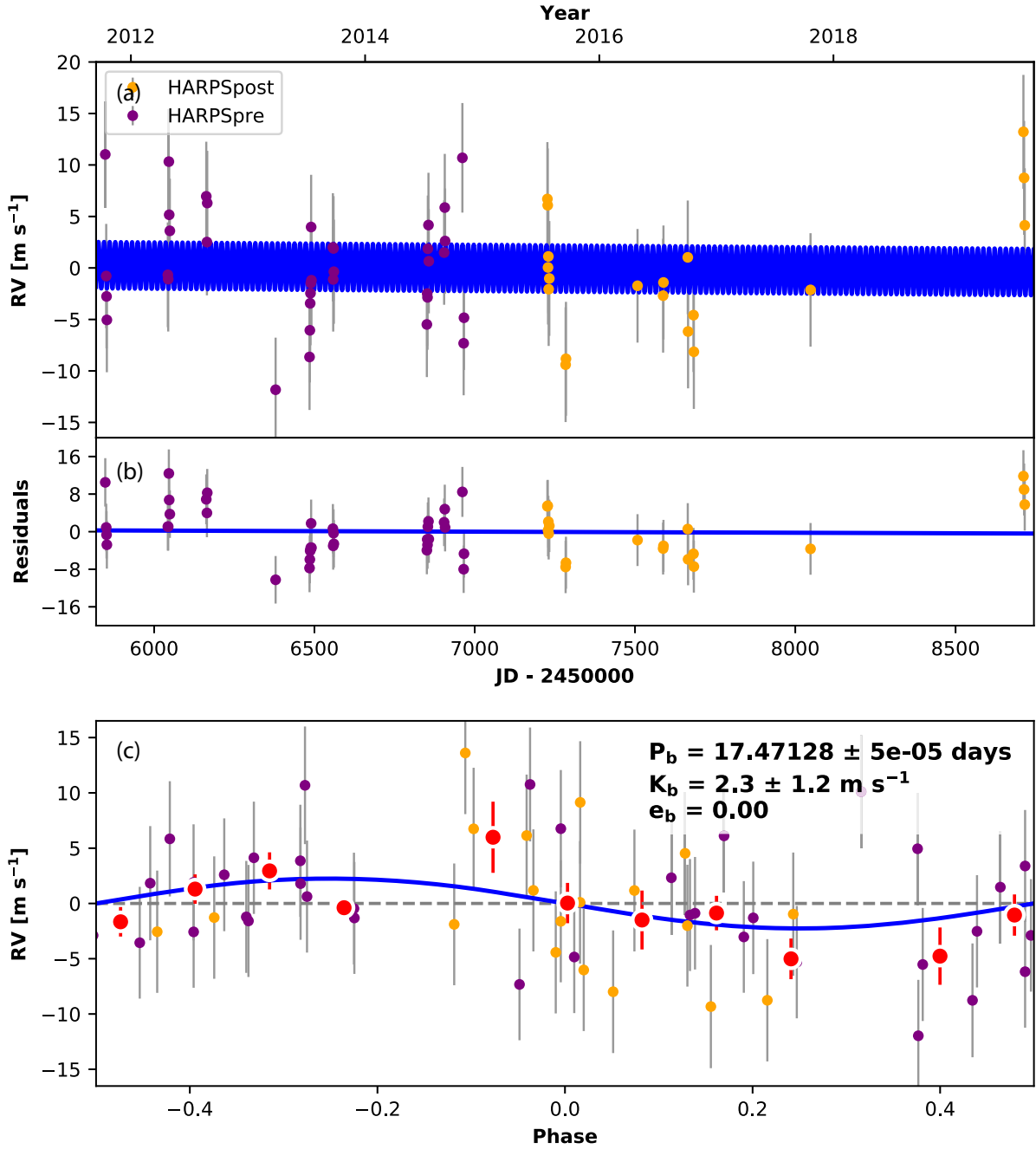ted in the bottom panel. The red points are the binned RVs. After including the new HARPS data, the model prefers a null RV slope (see Section 6.4).

[1]*Department of Astronomy and Tsinghua Centre for Astrophysics, Tsinghua University, Beijing 100084, China*

[2]*Center for Computational Astrophysics, Flatiron Institute, 162 Fifth Ave, New York, NY 10010, USA*

[3]*Departamento de Astronomia, IAG, Universidade de São Paulo, Rua do Matão 1226, São Paulo 05509-900, Brazil*

[4]*National Astronomical Observatories, Chinese Academy of Sciences, 20A Datun Road, Chaoyang District, Beijing 100012, China*

[5]*Department of Physics and Astronomy, Vanderbilt University, 6301 Stevenson Center Ln., Nashville, TN 37235, USA*

[6]*Department of Physics, Fisk University, 1000 17th Avenue North, Nashville, TN 37208, USA*

[7]*NASA Ames Research Center, Moffett Field, CA 94035, USA*

[8]*Department of Physics, Engineering and Astronomy, Stephen F. Austin State University, 1936 North St, Nacogdoches, TX 75962, USA*

[9]*Centre for Astrophysics, University of Southern Queensland, West Street, Toowoomba, QLD 4350 Australia*

[10]*Astrophysics Group, Keele University, Staffordshire ST5 5BG, UK*

[11]*Center for Astrophysics | Harvard & Smithsonian, 60 Garden Street, Cambridge, MA 02138, USA*

[12]*Department of Physics and Kavli Institute for Astrophysics and Space Research, Massachusetts Institute of Technology, Cambridge, MA 02139, USA*
[13]*Department of Earth, Atmospheric and Planetary Sciences, Massachusetts Institute of Technology, Cambridge, MA 02139, USA*
[14]*Department of Aeronautics and Astronautics, MIT, 77 Massachusetts Avenue, Cambridge, MA 02139, USA*
[15]*Department of Astrophysical Sciences, Princeton University, 4 Ivy Lane, Princeton, NJ 08544, USA*
[16]*Department of Astronomy, University of Florida, 211 Bryant Space Science Center, Gainesville, FL 32611, USA*
[17]*NASA Goddard Space Flight Center, 8800 Greenbelt Road, Greenbelt, MD 20771, USA*
[18]*University of Maryland, Baltimore County, 1000 Hilltop Circle, Baltimore, MD 21250, USA*
[19]*Department of Astronomy and Astrophysics, University of Chicago, 5640 S. Ellis Ave, Chicago, IL 60637, USA*
[20]*Department of Astronomy, The University of Texas at Austin, Austin, TX 78712, USA*
[21]*Cerro Tololo Inter-American Observatory, Casilla 603, La Serena, Chile*
[22]*Department of Physics & Astronomy, University of Kansas, 1082 Malott,1251 Wescoe Hall Dr., Lawrence, KS 66045, USA*
[23]*Max Planck Institute for Astronomy, Konigstuhl 17, D-69117 Heidelberg, Germany*
[24]*Department of Physics & Astronomy, Swarthmore College, Swarthmore, PA 19081, USA*
[25]*Department of Earth and Planetary Sciences, University of California, Riverside, CA 92521, USA*
[26]*Department of Physics and Astronomy, University of Louisville, Louisville, KY 40292, USA*
[27]*Department of Physics and Astronomy, The University of North Carolina at Chapel Hill, Chapel Hill, NC 27599-3255, USA*
[28]*NCCR/PlanetS, Centre for Space and Habitability, University of Bern, CH-3012 Bern, Switzerland*
[29]*George Mason University, 4400 University Drive MS 3F3, Fairfax, VA 22030, USA*
[30]*Patashnick Voorheesville Observatory, Voorheesville, NY 12186, USA*
[31]*Space Telescope Science Institute, 3700 San Martin Drive, Baltimore, MD 21218, USA*
[32]*SETI Institute, 189 Bernardo Ave, Suite 200, Mountain View, CA 94043, USA*
[33]*INAF – Osservatorio Astronomico di Padova, Vicolo dell'Osservatorio 5, I-35122 Padova, Italy*
[34]*Exoplanetary Science at UNSW, School of Physics, UNSW Sydney, NSW 2052, Australia*
[35]*Tsinghua International School, Beijing 100084, China*
[36]*Stanford Online High School, 415 Broadway Academy Hall, Floor 2, 8853, Redwood City, CA 94063, USA*
[37]*School of Astronomy and Space Science, Key Laboratory of Modern Astronomy and Astrophysics in Ministry of Education, Nanjing University, Nanjing 210046, Jiangsu, China*

This paper has been typeset from a TEX/LATEX file prepared by the author.